

AD A 169160

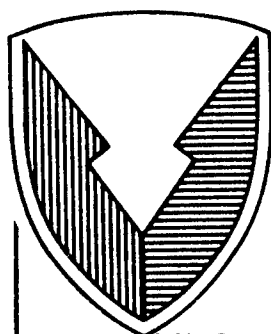
1018

A169160

# R D & E

C E N T E R

## Technical Report



No. 13077

SCANNING PHOTOACOUSTIC MICROSCOPY

OF

ALUMINUM WITH ALUMINUM OXIDE, ROUGHNESS STANDARDS,

AND

RUBBER

CONTRACT NUMBER DAAE 07-81-C-49-4049

AND MODIFICATIONS P00001 TO P00011

JULY 1985

R.L. Thomas, L.D. Favro, P.K. Kuo  
Wayne State University  
Detroit, MI 48202

By

D.N. Rose, D.C. Bryk, M. Chaika, J. Patt  
U.S. Army Tank-Automotive Command  
ATTN: AMSTA-RSA  
Warren, MI 48397-5000

U.S. ARMY TANK-AUTOMOTIVE COMMAND  
RESEARCH, DEVELOPMENT & ENGINEERING CENTER  
Warren, Michigan 48397-5000

20020726115

# NOTICES

This report is not to be construed as an official Department of the Army position.

Mention of any trade names or manufacturers in this report shall not be construed as an official endorsement or approval of such products or companies by the U.S. Government.

Destroy this report when it is no longer needed. Do not return it to the originator.

UNCLASSIFIED

SECURITY CLASSIFICATION OF THIS PAGE

## REPORT DOCUMENTATION PAGE

1a. REPORT SECURITY CLASSIFICATION UNCLASSIFIED			1b. RESTRICTIVE MARKINGS NONE	
2a. SECURITY CLASSIFICATION AUTHORITY			3. DISTRIBUTION / AVAILABILITY OF REPORT Approved for public release Distribution unlimited.	
2b. DECLASSIFICATION / DOWNGRADING SCHEDULE				
4. PERFORMING ORGANIZATION REPORT NUMBER(S)			5. MONITORING ORGANIZATION REPORT NUMBER(S)	
6a. NAME OF PERFORMING ORGANIZATION Wayne State University		6b. OFFICE SYMBOL (if applicable)	7a. NAME OF MONITORING ORGANIZATION US Army Tank-Automotive Command Research and Development Center	
6c. ADDRESS (City, State, and ZIP Code) Detroit, MI 48202			7b. ADDRESS (City, State, and ZIP Code) ATTN: AMSTA-ZSA Warren, MI 48397-5000	
8a. NAME OF FUNDING / SPONSORING ORGANIZATION		8b. OFFICE SYMBOL (if applicable)	9. PROCUREMENT INSTRUMENT IDENTIFICATION NUMBER DAAE07-81-C-4049	
8c. ADDRESS (City, State, and ZIP Code)			10. SOURCE OF FUNDING NUMBERS	
			PROGRAM ELEMENT NO.	PROJECT NO.
			TASK NO.	WORK UNIT ACCESSION NO.
11. TITLE (Include Security Classification) Scanning Photoacoustic Microscopy of Aluminum with Aluminum Oxide, Roughness Standards and Rubber				
12. PERSONAL AUTHOR(S) R. L. THOMAS, L.D. Favro, P. K. KUO, D.N. ROSE, D.C. BRYK, M. CHAIKA				
13a. TYPE OF REPORT FINAL REPORT		13b. TIME COVERED FROM Jun 84 TO Jun 85	14. DATE OF REPORT (Year, Month, Day) 85, July, 10	
15. PAGE COUNT				
16. SUPPLEMENTARY NOTATION The views, opinions, and/or findings contained in this report are those of the authors and shall not be construed as an official Department of the Army position, policy, or decision so designated by other documentation.				
17. COSATI CODES			18. SUBJECT TERMS (Continue on reverse if necessary and identify by block number)	
FIELD	GROUP	SUB-GROUP	Photoacoustic Microscopy, SPAM, Nondestructive Testing, Rubber, Thermal Wave Imaging, Ceramics	
19. ABSTRACT (Continue on reverse if necessary and identify by block number) Scanning photoacoustic microscopy (SPAM) and related thermal wave imaging techniques are emerging as methods of nondestructive evaluation (NDE), applicable to surface and near-surface characterization. The usefulness of these methods results from sensitivity to thermal properties, such as diffusivity and boundary conditions, near the point of the surface being probed. Through this sensitivity to localized thermal properties, SPAM can examine beneath the surface of an opaque material for voids, closed or open cracks, and inclusions. The maximum probe depth is approximately 2 mm, and the technique is particularly sensitive to flaws at depths from about 1 micron to 300-microns. The probe depth can be controlled experimentally. SPAM is also well suited to automatic data acquisition.  Some applications of SPAM and related thermal wave techniques to the studies of: aluminum with dispersed $Al_2O_3$ particles; surface roughness standards; and rubber track shoe pad material have been described in Interim Report No. 12668, July 1982. Similar applications				
20. DISTRIBUTION / AVAILABILITY OF ABSTRACT <input checked="" type="checkbox"/> UNCLASSIFIED/UNLIMITED <input type="checkbox"/> SAME AS RPT. <input type="checkbox"/> DTIC USERS			21. ABSTRACT SECURITY CLASSIFICATION UNCLASSIFIED	
22a. NAME OF RESPONSIBLE INDIVIDUAL DOUGLAS ROSE			22b. TELEPHONE (Include Area Code) (313) 574-7752	22c. OFFICE SYMBOL AMSTA-ZSA

## Block 19 (Continued)

for thermal wave images for color encoding at TACOM; coated samples; surface geometry; and dispersion in rubber samples have been described in Interim Report No. 12957, June 1984.

In this final report, the best photoacoustic detection techniques for imaging intrinsic rubber structure; thermal wave studies ceramic coated samples; thermal wave imaging of hollow turbine blades; and the capabilities of photoacoustic microscopy of monolithic silicon nitride and silicon carbide ceramics are discussed.

## SUMMARY

Scanning photoacoustic microscopy (SPAM) and related thermal wave imaging techniques are emerging as methods of non-destructive evaluation (NDE), applicable to surface and near-surface characterization. The usefulness of these methods results from sensitivity to thermal properties, such as diffusivity and boundary conditions, near the point on the surface being probed. Through this sensitivity to localized thermal properties, scanning photoacoustic microscopy can examine beneath the surface of an opaque material for voids, closed or open cracks, and inclusions. The maximum probe depth is approximately 2 mm, and the technique is particularly sensitive to flaws at depths from about 1 micron to 300 microns. The probe depth can be controlled experimentally. SPAM is also well suited to automatic data acquisition.

Some applications of SPAM and related thermal wave techniques to the studies of: aluminum with dispersed  $Al_2O_3$  particles; surface roughness standards; and rubber track shoe pad material have been described in the Interim Report No. 12668, July, 1982. Similar applications for: thermal wave images for color encoding at TACOM; coated samples; surface geometry; and dispersion in rubber samples have been described in the Interim Report No. 12957, June, 1984.

In this final report, the best photoacoustic detection techniques for imaging intrinsic rubber structure; thermal wave studies of ceramic coated samples; thermal wave imaging of hollow turbine blades; and the capabilities of photoacoustic microscopy on monolithic silicon nitride and silicon carbide ceramics are discussed.

## PREFACE

This work was performed by Wayne State University, Detroit, MI 48202 for the US Army Tank-Automotive Command (TACOM). Army Research Physicist Douglas Rose of TACOM, Warren, MI, directed the administration of the effort. It was performed at the Department of Physics and Astronomy of Wayne State University with Professor R. L. Thomas as principal investigator, in collaboration with Professor L. D. Favro and Professor P. K. Kuo.

This project was accomplished with funds from the US Army Research Office through Dr. Fred Schmeideshof to TACOM for establishing Scanning Photoacoustic Microscopy (SPAM) as a nondestructive evaluation tool, from the Readiness for Reliability Program under Mr. Paul Doyle and Mr. Jim Kidd of the US Army Materials Technology Laboratory (MTL), which was then titled Army Materials and Mechanics Research Center, (AMMRC), from an MTT Program under Mr. Robert Brockelman, also of MTL, and with funds from the Track Elastomer Program through Mr. Jacob Patt of TACOM.

The authors gratefully acknowledge the technical assistance provided by L. J. Inglehart, K. R. Grice, J. Lhota, I. Bergel, C. Reyes, W. Shen, S. Munidasa and Z. J. Feng in the SPAM experiments.

## TABLE OF CONTENTS

<u>Section</u>	<u>Page</u>
1.0. INTRODUCTION	9
1.1. Applications	9
1.2. Technical Principles	9
1.2.1. Thermal Wave Generation	9
1.2.2. Thermal Wave Signal Detection Methods	10
1.3. Comparison of Methods	10
1.4. Data Collection and Processing	10
2.0. TECHNIQUES FOR IMAGING INTRINSIC RUBBER STRUCTURE	11
2.1. Data Link Between Wayne State and TACOM	11
2.2. Images Encoded	11
2.3. Subsurface Defect in Rubber Sample ABR	16
2.4. Samples of Good Dispersion and Poor Dispersion Rubber	16
2.5. Thermal Wave Images of Good Dispersion and Poor Dispersion Rubber	24
3.0. STUDIES OF CERAMIC-COATED SAMPLES	24
3.1. Thermal Wave Images of Ceramic-Coated SiC-6	24
3.2. Thermal Diffusivity Measurements of Ceramic-Coated SiC-6	24
4.0. IMAGING OF HOLLOW TURBINE BLADES	31
5.0. MONOLITHIC $\text{Si}_3\text{N}_4$ AND SiC CERAMICS	44
5.1. Specimens	44
5.2. Thermal Wave Images of Monolithic Ceramics	45
6.0. RECOMMENDATIONS	45
6.1. Intrinsic Rubber Structure	45
6.2. Ceramic-coated Samples	54
6.3. Hollow Turbine Blades	54
6.4. Monolithic $\text{Si}_3\text{N}_4$ and SiC Samples	54
LIST OF REFERENCES	55

## LIST OF FIGURES

<u>Figure No.</u>	<u>Title</u>	<u>Page</u>
1.	Photoacoustic microscope thermal wave images of a brittle fracture region beneath a Knoop-indented SiC surface at a frequency of 1 kHz. The four segments of the figure are successive scans of the same region of the sample with four different settings of the phase of the lock-in amplifier. A detailed description is given in Ref. 3.	12
2.	An optical image (top), Gas-cell thermal wave magnitude (middle), and a MIRAGE thermal wave image (lower) of an open, nearly vertical fatigue crack in an aluminum alloy. A detailed description is given in Ref. 7.	13
3.	Composite optical and SPAM micrographs of a 400 x 400 point region of an aluminum alloy containing fatigue cracks which are apparently smaller in length than our present detection capability ( $\sim 30\mu\text{m}$ ). A detailed description is given in Ref. 7.	14
4.	SPAM magnitude and phase perspective plots (top) and gray scale images (bottom) of a $45^\circ$ slanted fabricated crack in an aluminum alloy. A detailed description is given in Ref. 9.	15
5.	Schematic diagram of Rubber ABR sample with prepared subsurface defects.	17
6.	Schematic diagram of cylindrically-shaped subsurface defects in Rubber ABR sample.	18
7.	Frequency dependence of thermal wave MIRAGE effect, normal deflection magnitude signals for the Rubber ABR cylindrical hole with air (see Fig. 6).	19
8.	Frequency dependence of thermal wave MIRAGE effect, normal deflection magnitude signals for the Rubber ABR cylindrical hole filled with aluminum powder (see Fig. 6).	20
9.	Frequency dependence of thermal wave MIRAGE effect, normal deflection magnitude signals for the Rubber ABR cylindrical hole filled with an aluminum rod (see Fig. 6).	21



10.	Frequency dependence of thermal wave MIRAGE effect, normal deflection phase signals for the Rubber ABR cylindrical hole filled with an aluminum rod (see Fig. 6).	22
11.	Thermal wave MIRAGE effect image at a frequency of 100 Hz, using the normal deflection magnitude signal, of a 2.54 mm x 2.54 mm area of the surface of the Rubber ABR sample above the cylindrical hole filled with an aluminum rod (see Fig. 6).	23
12.	Representative MIRAGE thermal wave and scanned optical images of Rubber Sample 901-83A (pure gum of peroxide and synthetic polyisoprene) [ a) 400 Hz scanned optical; b) 400 Hz MIRAGE magnitude; c) 400 Hz MIRAGE phase; d) 1 kHz MIRAGE magnitude; e) 1 kHz MIRAGE phase].	25
13.	Representative MIRAGE thermal wave and scanned optical images of Rubber Sample 901-83C (10 phr N326, low structure HAF, good dispersion) [ a) 400 Hz scanned optical; b) 400 Hz MIRAGE magnitude; c) 400 Hz MIRAGE phase; d) 1 kHz MIRAGE magnitude; e) 1 kHz MIRAGE phase].	26
14.	Representative MIRAGE thermal wave and scanned optical images of Rubber Sample 901-83B (10 phr N326, poor dispersion) [ a) 400 Hz scanned optical; b) 400 Hz MIRAGE magnitude; c) 400 Hz MIRAGE phase; d) 1 kHz MIRAGE magnitude; e) 1 kHz MIRAGE phase].	27
15.	Representative MIRAGE thermal wave and scanned optical images of Rubber Sample 901-83E (10 phr Coarse Whiting, calcium carbonate, good dispersion) [ a) 400 Hz scanned optical; b) 400 Hz MIRAGE magnitude; c) 400 Hz MIRAGE phase; d) 1 kHz MIRAGE magnitude; e) 1 kHz MIRAGE phase].	28
16.	Representative MIRAGE thermal wave and scanned images of Rubber Sample 901-83D (10 phr Coarse Whiting, poor dispersion [ a) 400 Hz scanned optical; b) 400 Hz MIRAGE magnitude; c) 400 Hz MIRAGE phase; d) 1 kHz MIRAGE magnitude; e) 1 kHz MIRAGE phase].	29
17.	Thermal wave MIRAGE thermal wave and scanned optical images of five different regions on the same ceramic-coated sample (Sample 1-ND, a CVD SiC coating 0.003" thick on a substrate of SiC-6).	30

18.	Line traces showing the frequency dependence of the zero crossings (x) for the in-phase component of the transverse MIRAGE deflection for a single crystal of InSb.	32
19.	A graph of the measured zero crossings (x) for Cu, Al, SiC, In, Si <sub>3</sub> N <sub>4</sub> , and InSb, plotted as a function of inverse-square-root frequency. The measured slopes give values for the thermal diffusivities of these materials that are in good agreement with those found in the literature.	33
20.	A graph of the measured zero crossings (x) for a coated nickel-based superalloy (IN 738) plotted as a function of inverse-square-root frequency, for both the coated and uncoated portions of the sample.	34
21.	A graph of the measured zero crossings (x) for ceramic-coated sample 1-ND (0.003" coating of CVD SiC on a SiC-6 substrate).	35
22.	A graph of the measured zero crossings (x) for ceramic-coated sample 1-ND (0.0033" coating of CVD SiC on a ZrO <sub>2</sub> substrate).	36
23.	A graph of the measured zero crossings (x) for ceramic-coated sample 2-A (0.0058" coating of CVD SiC on a ZrO <sub>2</sub> substrate).	37
24.	A graph of the measured zero crossings (x) for ceramic-coated sample 3-B (0.007" coating of CVD SiC on a ZrO <sub>2</sub> substrate).	38
25.	A graph of the measured zero crossings (x) for ceramic-coated sample 1-A (0.0013" coating of CVD SiC on a ZrO <sub>2</sub> substrate).	39
26.	Theory for the thermal wave scattering from a subsurface cylinder of much lower thermal diffusivity than the host material.	40
27.	Experimental results for the thermal wave scattering from a subsurface cylinder of much lower thermal diffusivity than the host material.	41
28.	Thermal wave MIRAGE (magnitude of the normal deflection) image of two cooling air holes at the trailing edge of aTF30 first stage turbine blade at a frequency of 5.4 Hz (compare with Figs. 26 and 27)	42

29.	Thermal wave MIRAGE (magnitude of the normal deflection at 100 Hz) image of a region of aTF30 first stage turbine blade for which previous radiographic studies had indicated the possible presence of subsurface defects.	43
30.	Thermal wave MIRAGE (magnitude and phase of the normal deflection at 1 kHz) and scanned optical images for the regularly machined surface (R) of silicon nitride Specimen No. 1. [ a) optical; b) MIRAGE magnitude; c) MIRAGE phase].	46
31.	Thermal wave MIRAGE (magnitude and phase of the normal deflection at 1 kHz) and scanned optical images for the degraded surface (D) of silicon nitride Specimen No. 1 [ a) optical; b) MIRAGE magnitude; c) MIRAGE phase].	47
32.	Thermal wave MIRAGE (magnitude and phase of the normal deflection at 1 kHz) and scanned optical images for the regularly machined surface (R) of silicon carbide Specimen No. 2 [ a) MIRAGE magnitude; b) MIRAGE phase].	48
33.	Thermal wave MIRAGE (magnitude and phase of the normal deflection at 1 kHz) and scanned optical images for the degraded surface (D) of silicon carbide Specimen No. 2. [ a) optical; b) MIRAGE magnitude; c) MIRAGE phase].	49
34.	Thermal wave MIRAGE (magnitude and phase of the normal deflection at 4 kHz) and scanned optical images for the heat-treated specimen of silicon carbide (Specimen No. 3) [ a) optical; b) MIRAGE magnitude; c) MIRAGE phase].	50
35.	Thermal wave MIRAGE (in-phase component of the transverse deflection at 1 kHz) and scanned optical images for the Knoop indented surfaces of silicon nitride Specimen No. 4 [ top: 2.7 kG load indentation crack; bottom: 1.7 kG load indentation crack].	51
36.	Thermal wave MIRAGE (in-phase component of the transverse deflection at 1 kHz) and scanned optical images for the Knoop indented surfaces of silicon carbide Specimen No. 5 [ top: 2.7 kG load indentation crack; bottom: 1.7 kG load indentation crack].	52

## 1.0. INTRODUCTION

### 1.1. Applications.

Scanning Photoacoustic Microscopy (SPAM) is an emerging nondestructive evaluation (NDE) technique, initiated at Wayne State University.<sup>1</sup> It is applicable to surface and near surface characterization. Research in our laboratory and elsewhere<sup>1-10</sup> is establishing the experimental and theoretical framework for interpreting SPAM micrographs for a variety of subsurface defects. These include a simulated subsurface void<sup>5</sup>, delaminations in layered structures<sup>6</sup>, closed, lateral subsurface cracks<sup>7,8</sup>, and closed slanted cracks.<sup>9</sup> SPAM has also<sup>10</sup> been applied to complex shaped parts such as turbine engine components.

### 1.2. Technical Principles.

1.2.1. Thermal Wave Generation. Detailed descriptions of SPAM and its potential for nondestructive evaluation (NDE) applications are given in the literature.<sup>1-10</sup> Essentially, the technique may be thought of as thermal wave imaging, where an intensity-modulated and focused laser beam (electron beams or ion beams may also be used) establishes a point source of heat which varies in time at the modulating (or "chopping") frequency. The beam is scanned over the sample surface to generate, one point at a time, a photoacoustic image.

The temperature (T) within the sample, beneath the point on the surface being probed, is a function of time (t) and depth (x). These variations can be modeled by solving the one-dimensional thermal diffusion equation for a semi-infinite solid whose temperature at the boundary is a periodic function of time. Assuming a sinusoidal variation, the steady-state solution is of the form

$$T(x,t) = T_0 \exp[i(qx - \omega t)],$$

where  $i = \text{square root of } -1$  and  $q, \omega$ , are explained below. The temperature in the solid is periodic in space and time. The space variable is a complex quantity with equal real and imaginary parts, so the thermal wave is very highly damped spatially. Significant temperature variations extend only to one or two multiples of the thermal wavelength. The thermal wavelength,  $\lambda_t = 2\pi/\text{Re}(q)$ , is defined as  $2\pi(2k/\omega\rho c)^{1/2}$ , where  $\omega/2\pi =$  the heat source modulating frequency, and  $k, \rho$ , and  $c$  are the thermal conductivity, density and heat capacity of the material. The thermal wave accordingly probes only the region close to the surface, the depth of which can be varied experimentally by adjusting the laser (or other heat source) modulation frequency. Typically, the probed depth can be varied experimentally from 100  $\mu\text{m}$  to  $\sim 2\text{mm}$ . Defects between the surface and that depth are detectable due to variation in thermal properties or discontinuities in thermal properties. Photoacoustic signals are also sensitive to variations in

surface conditions, as will be described as part of the present work.

1.2.2. Thermal Wave Signal Detection Methods. Thermal wave imaging can be performed with any of several thermal wave detection techniques. One method uses a sensitive microphone in conjunction with a gas cell surrounding the point being probed. As the point is alternately heated and cooled, it in turn heats and cools the air (or other gas) in its vicinity, generating an acoustic (sound) signal which the microphone detects. Another technique is optical mirage-effect detection (MIRAGE), whereby a separate laser probe beam is directed parallel to the material surface through the air above the point being probed. The gradient in optical index of refraction of the air, associated with the temperature gradient in the air, causes a deflection of the probe laser beam. This deflection is detected by a position sensor and is the MIRAGE signal.

Thermal wave signals generated by a microphone or probe laser system have both an amplitude and a phase (relative to the heating laser modulation). Thermal wave images can be generated by recording the amplitude or phase of the signal as a function of position as the relative position between the heating point and the surface of the material under study is scanned.

### 1.3. Comparison of Methods.

A detailed comparison of gas-cell and MIRAGE techniques for detecting slanted cracks has recently been carried out by the Wayne State research group. The results were that MIRAGE detection is especially useful in detecting vertical cracks, and has the advantage of noncontact with the surface being probed. This advantage is evident in the thermal wave images of cracks in monolithic silicon nitride and silicon carbide ceramics, presented in Section 5.0 of this report. A disadvantage of MIRAGE is that the geometry of the specimen must allow access by the probe beam, from source to detector, to a line nearly tangent to the surface at all points to be probed.

### 1.4. Data Collection and Processing.

These thermal wave scans are controlled by a microprocessor and digital data acquisition and storage techniques are employed. Most of the data presentations will be in the form of gray scale micrographs. These are generated by feeding a digital to analog (D/A) converter from the microprocessor memory and using the output to intensity-modulate the electron beam of a CRT display. The display is then photographed with an oscilloscope camera. In these photographs, typically a  $6.35 \mu\text{m} \times 6.35 \mu\text{m}$  pixel is used (1 step  $\times$  1 step of the x-y stages), resulting in 12,500 to 22,500 points. In some cases, where a larger area is to be scanned, a larger pixel is used. Since the gray scale resolution of the data (8 bits, or 256 gradations) considerably exceeds that of the CRT/film display, the authors have used computer-generated perspective plots in some cases. In addition, the high-resolution color graphics capability at TACOM was used to enhance the display of information generated by the SPAM process. In some instances (e.g., our earlier analysis of the roughness standards data<sup>13</sup>), a

microcomputer is used to analyze the data for comparison with conventional measurements of average properties.

In summary, SPAM is applicable for surface and near subsurface NDE, with a depth range which can be varied experimentally. The authors have calculated the thermal wave scattering expected theoretically from simple subsurface defects and found excellent agreement with experiments on fabricated defects in uniform materials. Characteristic signatures have been identified which allow these defects to be discriminated from one another. Thermal wave imaging is also well suited to automatic data acquisition.

## 2.0. TECHNIQUES FOR IMAGING INTRINSIC RUBBER STRUCTURE

### 2.1. Data Link Between Wayne State and TACOM.

In order to circumvent the limited gray scale resolution of the CRT/black and white film display, and to use more of the inherent resolution (8 bit) of the data, a digital data transfer link was established between the authors' laboratory at Wayne State University and TACOM. This enables thermal wave images to be transferred in a format which is compatible with the Hewlett-Packard computer system at the Survivability Research Division of TACOM's Tank-Automotive Concepts Laboratory. Images with at least 10,000 points (100 x 100) obtained from several different specimens have been transferred.

### 2.2. Images Encoded.

A perspective plot and conventional gray scale thermal wave images of four samples are presented in Figs. 1-4. Fig. 1 shows a four-phase perspective plot<sup>8</sup> of a brittle fracture region beneath a Knoop-indented SiC surface, where gas-cell detection was used. In each of the four separate plots in Fig. 1, the magnitude (height) at a given position represents the component of the photoacoustic signal projected along a phase-vector (phasor) with a given phase relative to the heating laser modulation. Hence, in the - 90 degree plot, the height at each point represents the value of that component of the photoacoustic signal which lags 90 degrees behind that for which the corresponding signal from the undamaged region is maximized.

The authors have demonstrated elsewhere<sup>8</sup> that this characteristic phase dependence is to be expected for thermal wave scattering from a field of closed, lateral cracks which are thermally close to the surface (depth  $\sim \lambda_t$ ). These images have also been displayed using the high-resolution color graphics monitor at TACOM.

Fig. 2 shows an optical image, two gas-cell thermal wave images (magnitude and phase), and a MIRAGE image of an open, nearly vertical fatigue crack in an aluminum alloy. Phase image refers to a thermal wave image where changes in phase, rather than of magnitude, of the received signal are recorded. Fig. 3 shows optical and gas-cell thermal wave images of another aluminum alloy, both of which are composites of a number of smaller images arranged

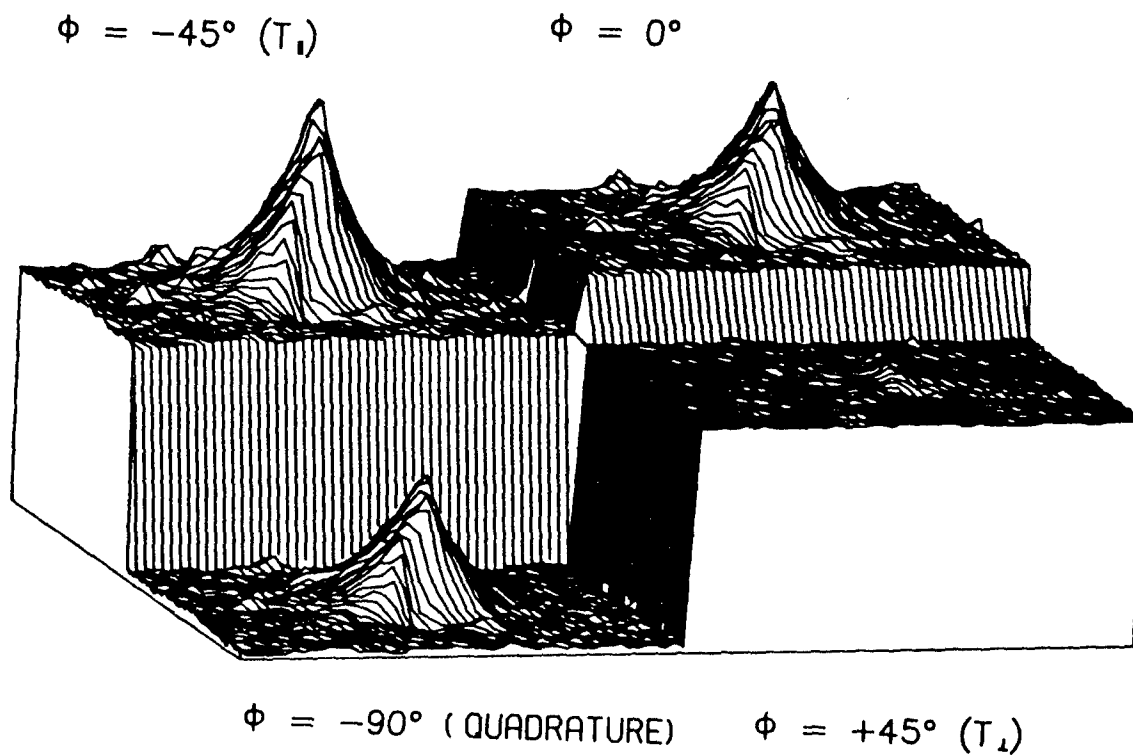


Fig. 1 Photoacoustic microscope (SPAM) thermal wave images of a brittle fracture region beneath a Knoop-indented SiC surface at a frequency of 1 kHz. The four segments of the figure are successive scans of the same region of the sample with four different settings of the phase of the lock-in amplifier. A detailed description is given in Ref. 3.

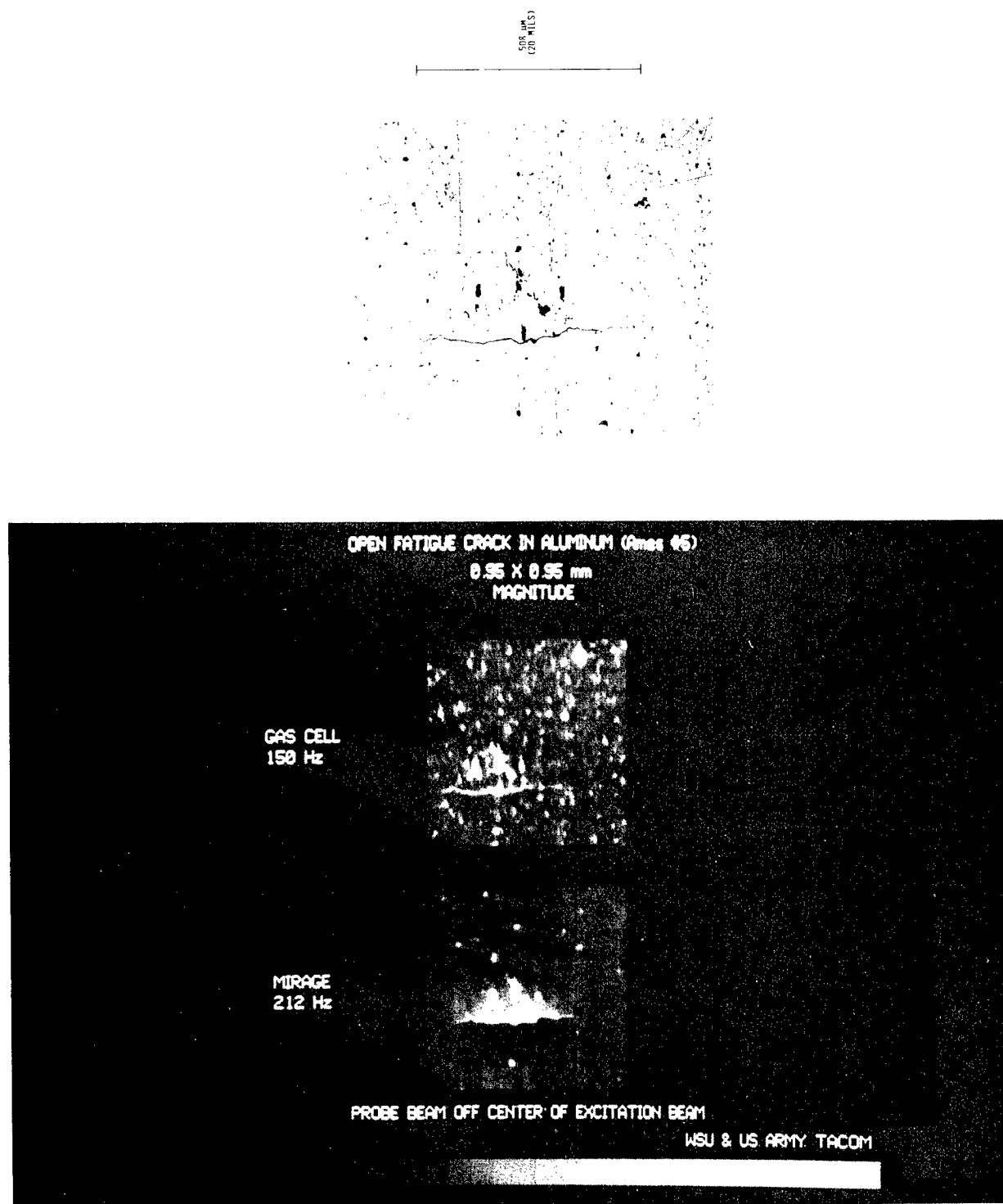


Fig. 2 An optical image (top), Gas-cell thermal wave magnitude (middle), and a MIRAGE thermal wave image (lower) of an open, nearly vertical fatigue crack in an aluminum alloy. A detailed description is given in Ref. 7.



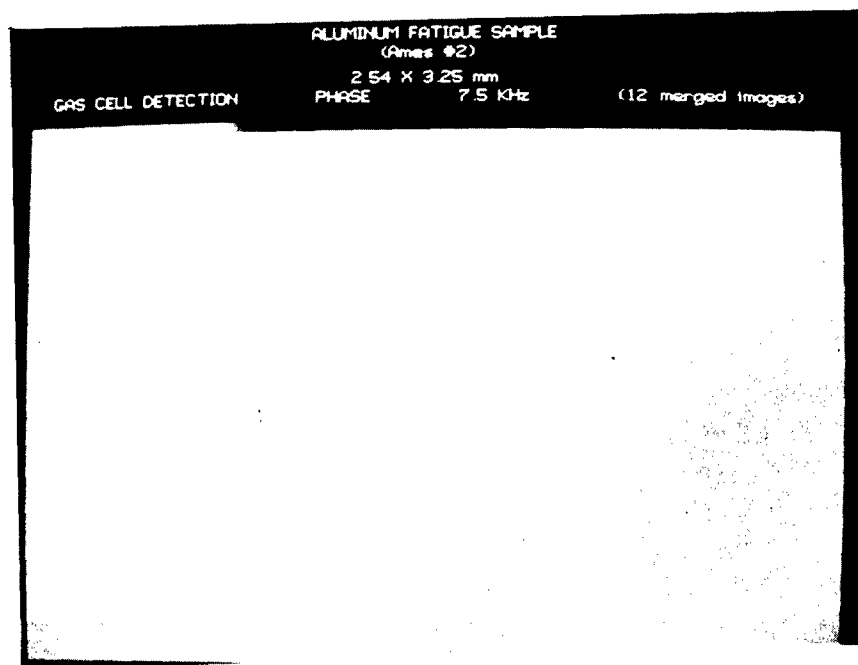
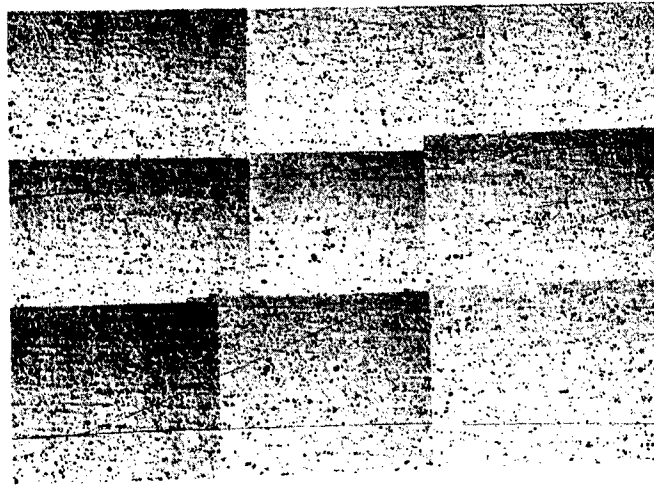


Fig. 3 Composite optical and SPAM micrographs of a 400 x 400 point region of an aluminum alloy containing fatigue cracks which are apparently smaller in length than our present detection capability ( $\sim 30 \mu\text{m}$ ). A detailed description is given in Ref. 7.

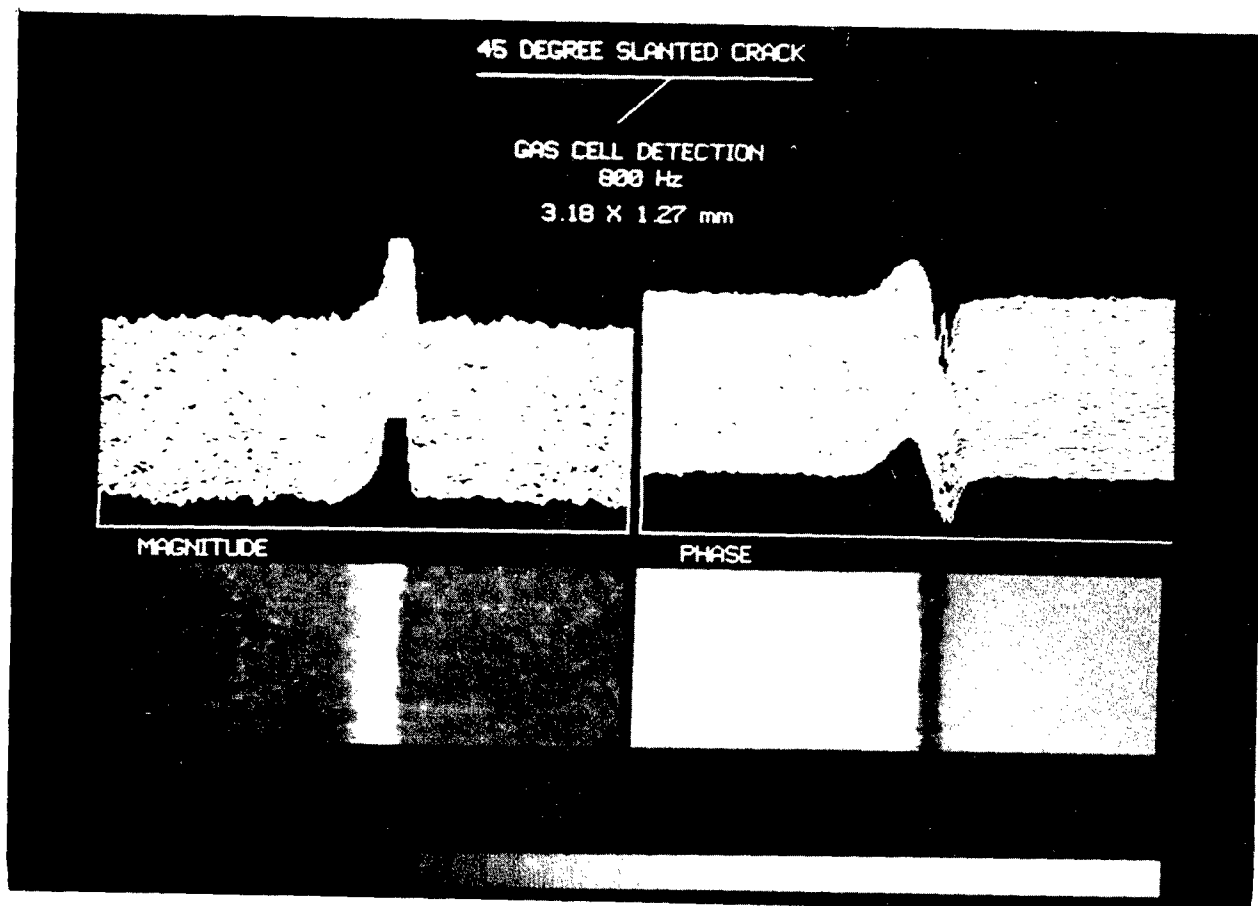


Fig. 4 SPAM magnitude and phase perspective plots (top) and gray scale images (bottom) of a  $45^{\circ}$  slanted fabricated crack in an aluminum alloy. A detailed description is given in Ref. 9.

to illustrate a 400 x 400 point region. This sample has fatigue cracks which are too short for our present detection capability ( $\sim 30 \mu\text{m}$ ). Color images have been prepared using the same thermal wave data, but the small cracks are still not detectable. Fig. 4 illustrates gas-cell magnitude and phase images as both gray scale images and perspective plots of a 45 degree slanted fabricated crack in an aluminum alloy, which have been explained theoretically in Reference 9. The crack is slanting in the direction indicated at the top of Fig. 4.

### 2.3. Subsurface Defect in Rubber Sample ABR

In order to determine the best photoacoustic detection techniques, we have carried out an experiment using the MIRAGE technique (normal deflection) to detect thermal wave scattering from specially prepared subsurface defects in a sample of Rubber ABR (Sample A, Black-loaded, Rough surface). These defect samples are described schematically in Figs. 5 and 6. Sample preparation consisted of : (1) Cutting a block of Rubber ABR to dimensions 18.0 mm x 16.5 mm x 3.91 mm, (2) Polishing both large faces of the rubber sample until smooth, (3) Cooling the sample to liquid nitrogen temperature and drilling several flat-bottomed holes with a 1/16" end-mill, and (4) carefully polishing the top surface to obtain the thinnest possible wall thicknesses to the subsurface holes. Some of the holes were left as air-filled holes, some were filled with aluminum powder, and others were filled with press-fitted aluminum rods, as depicted in Figs. 5 and 6.

Line scans of the normal deflection (magnitude and phase) of the optical probe beam as a function of position across the thin wall regions above the subsurface holes are shown in Figs. 7-10. From the frequency dependence of these scans from 2.5 Hz to about 100 Hz (above which the subsurface holes are essentially undetectable), it is demonstrated that thermal wave imaging of subsurface features in this material is indeed possible. The fact that very low modulation frequencies are required is entirely consistent with the known poor thermal diffusivity of rubber (we have also confirmed this conclusion using transverse deflection measurements<sup>14</sup> of the thermal diffusivity of Rubber Sample 901-83C, described below). This also makes clear the advantage of optical detection, which can be carried out at frequencies as low as 1 Hz. An area scan of one of the aluminum-rod-filled subsurface holes is shown in Fig. 11.

### 2.4. Samples of Good Dispersion and Poor Dispersion Rubber

The following rubber samples (fabricated by Mr. J.R. Beatty, 2102 Wyndham Road, Akron, Ohio 44313) were supplied by TACOM for thermal wave imaging dispersion studies:

1. Pure gum of peroxide and synthetic polyisoprene  
(Sample 901-83A)
2. 10 phr N326 (low structure HAF) good dispersion  
(Sample 901-83C)

# First Lapping

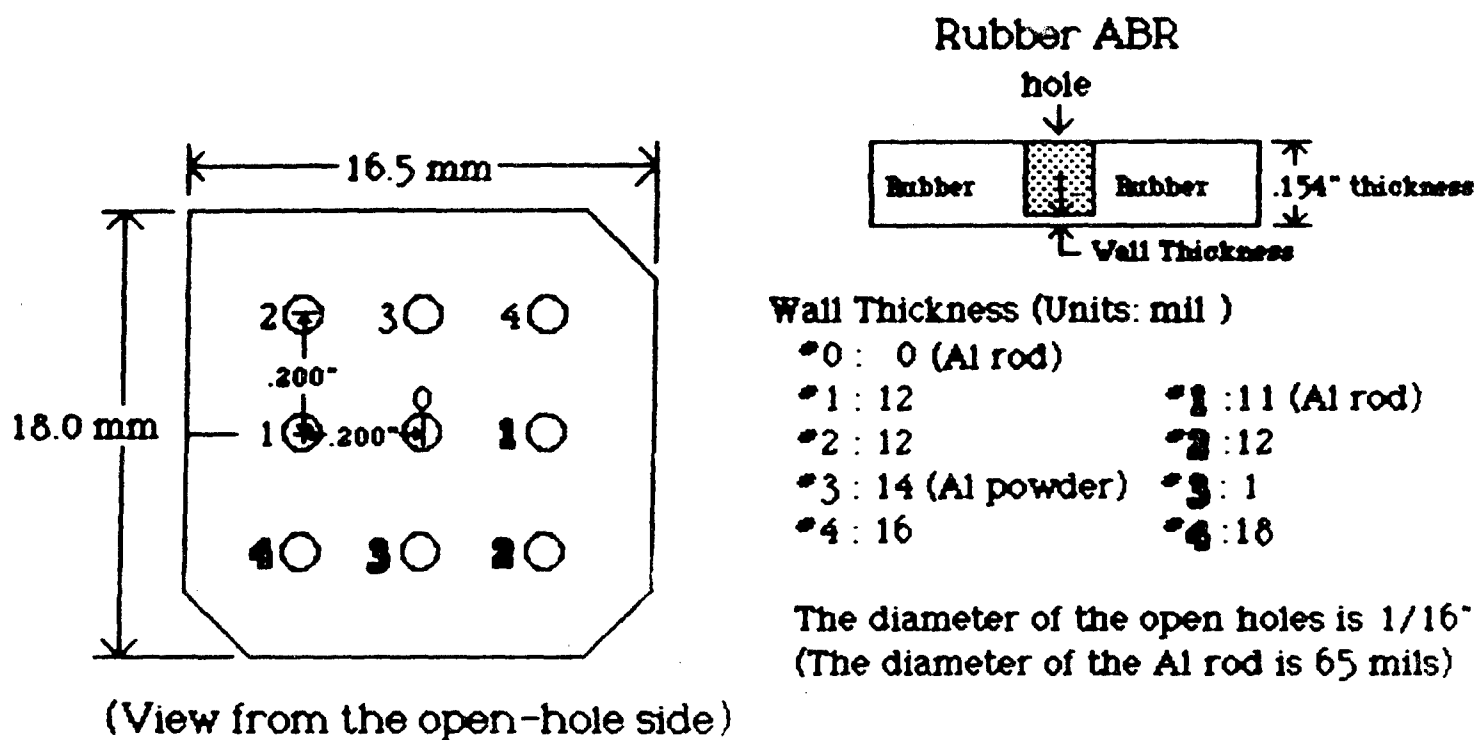


Fig. 5. Schematic diagram of Rubber ABR sample with prepared subsurface defects.

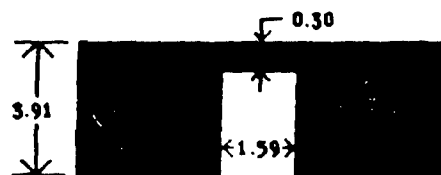
### Sample Preparation:

- (1) A sample of 18.0mm x 16.5mm x 3.91 mm is cut from a ABR rubber block.
- (2) Both faces of the block are polished until smooth.
- (3) The sample is kept liquid-nitrogen-

cooled while several holes are drilled with an end mill of 1/16".

- (4) The upper face of the sample is lapped and polished to the possible thinnest wall thickness.

#### Cylindrical Hole with Air

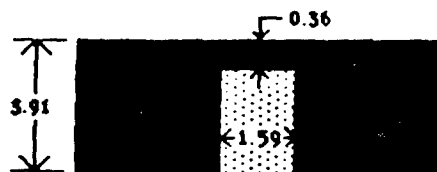


(Unit : mm)

Hole Diameter : 1.59 mm (0.0625")

Wall Thickness : 0.30 mm (0.012")

#### Cylindrical Hole with Al Powder

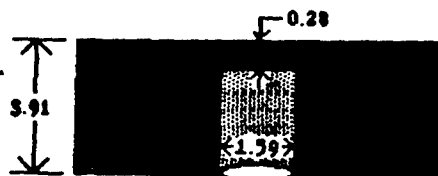


(Unit : mm)

Hole Diameter : 1.59 mm (0.0625")

Wall Thickness : 0.36mm (0.014")

#### Cylindrical Hole press filled with Al Rod



(Unit : mm)

Hole diameter : 1.59mm (0.0625")

Al-rod diameter : 1.65mm (0.0627")

Wall thickness : 0.28mm (0.011")

Fig. 6. Schematic diagram of cylindrical-shaped subsurface defects in Rubber ABR sample

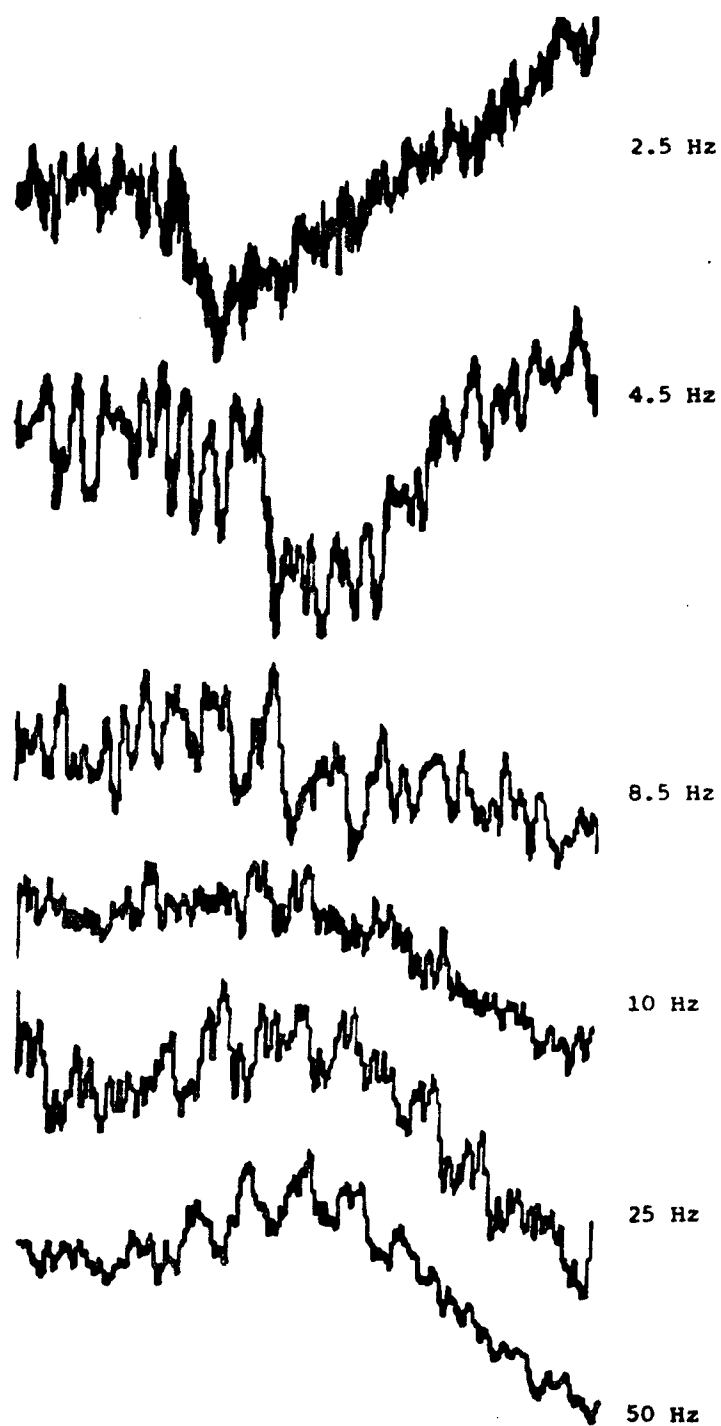


Fig. 7. Frequency dependence of thermal wave MIRAGE effect, normal deflection magnitude signals for the Rubber ABR cylindrical hole with air (see Fig. 6). The length of the scans is 2.54 mm.

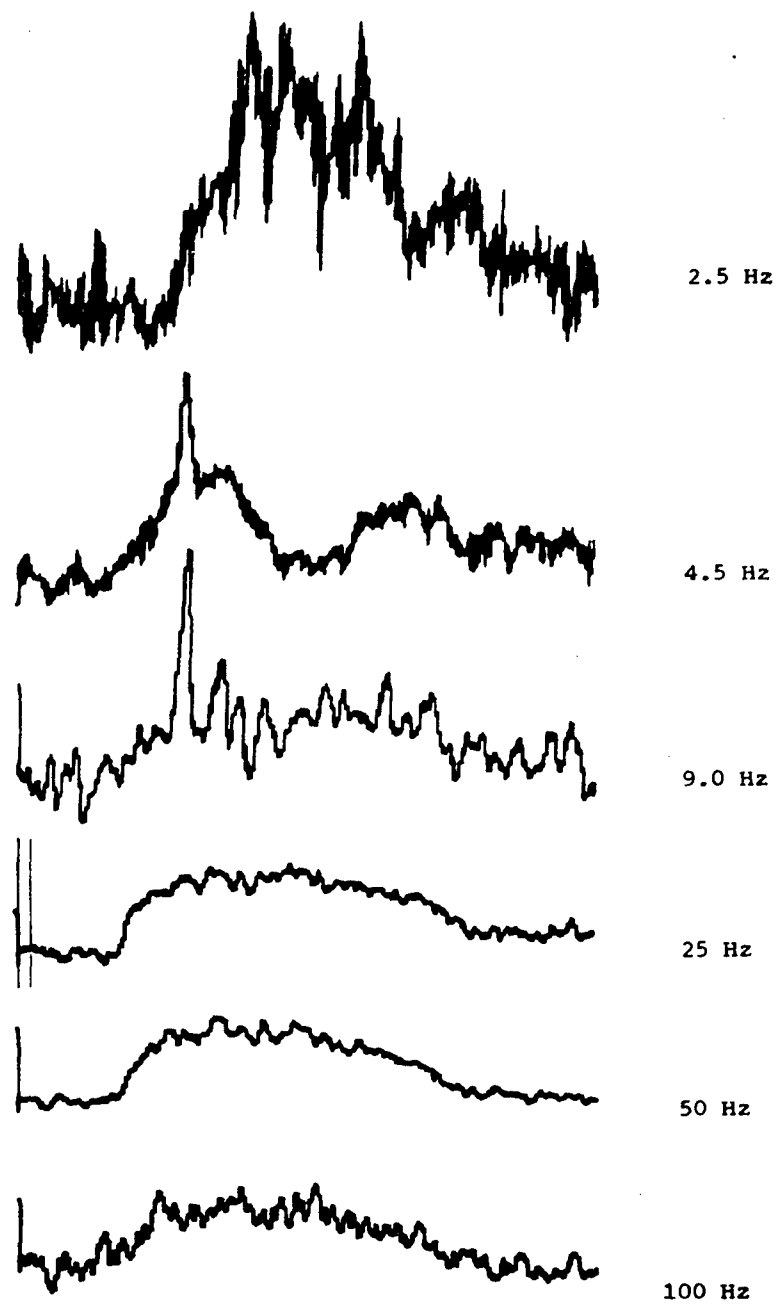


Fig. 8. Frequency dependence of thermal wave MIRAGE effect, normal deflection magnitude signals for the Rubber ABR cylindrical hole filled with aluminum powder (see Fig. 6). The length of the scans is 2.54 mm.

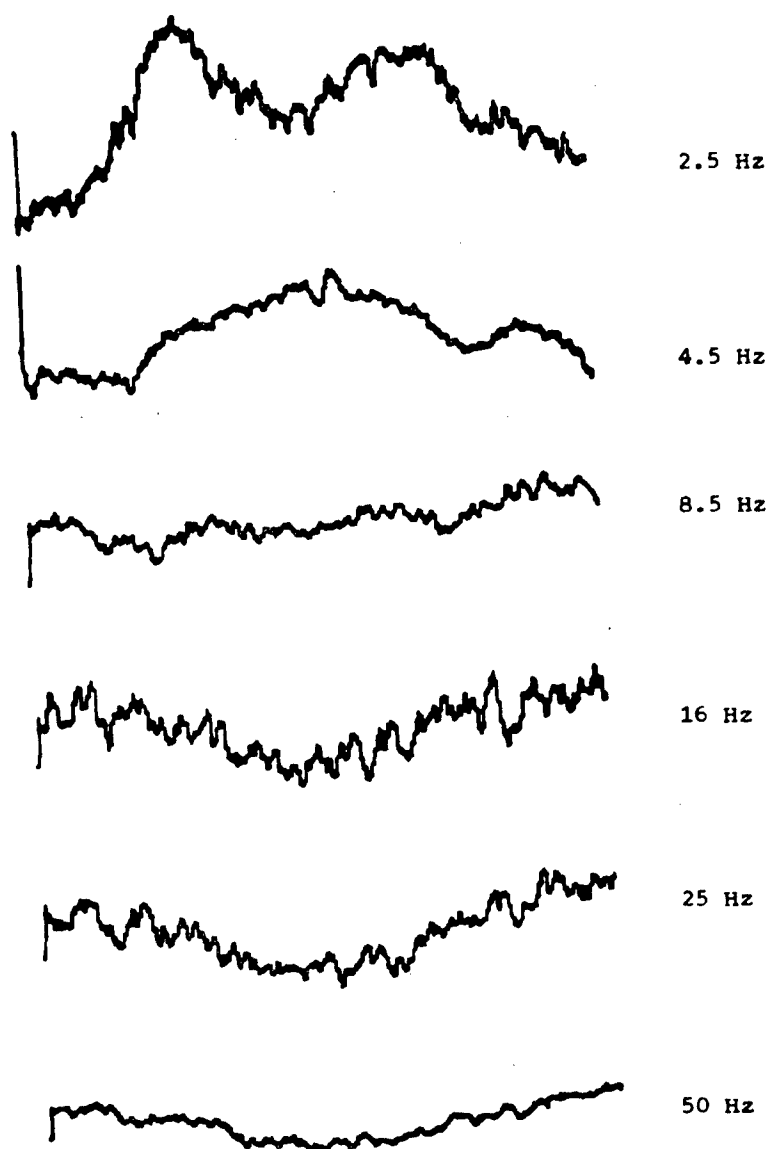


Fig. 9. Frequency dependence of thermal wave MIRAGE effect, normal deflection magnitude signals for the Rubber ABR cylindrical hole filled with an aluminum rod (see Fig. 6). The length of the scans is 2.54 mm.



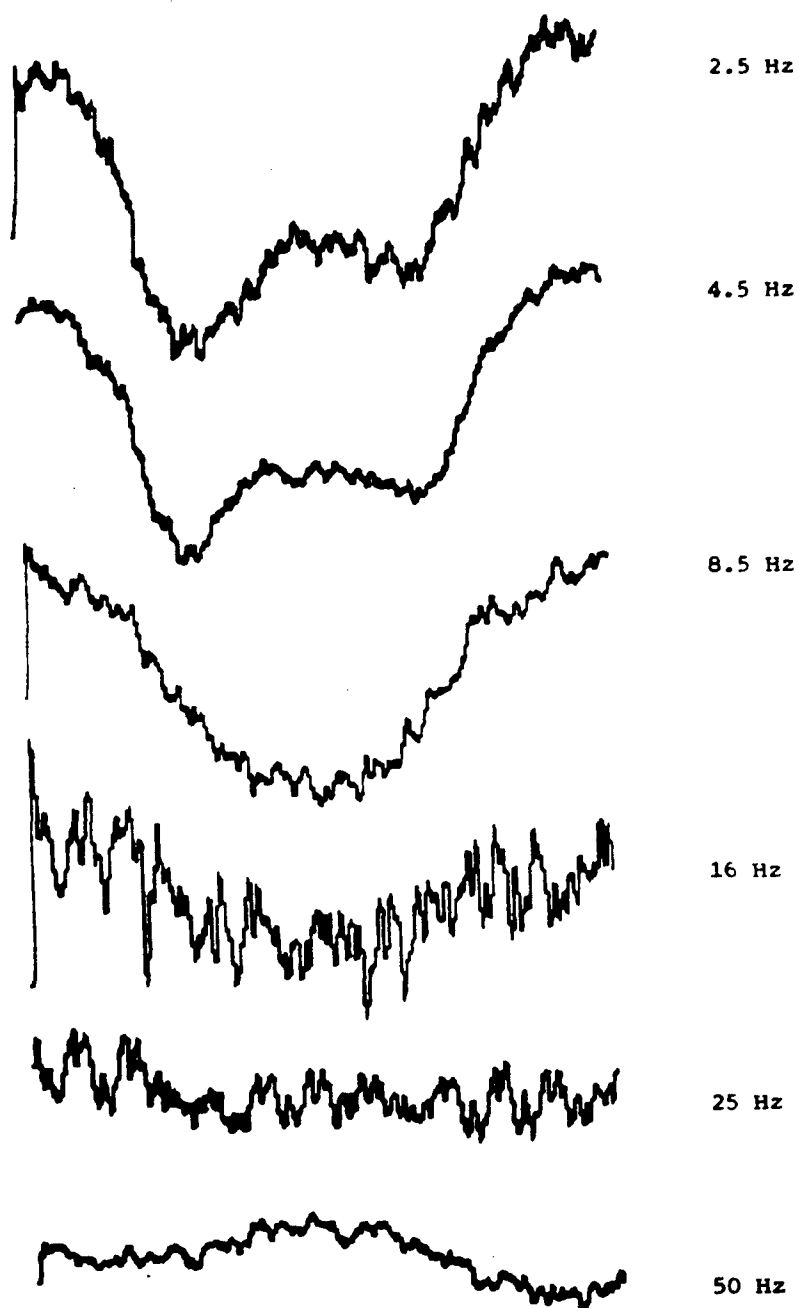


Fig. 10. Frequency dependence of thermal wave MIRAGE effect, normal deflection phase signals for the Rubber ABR cylindrical hole filled with an aluminum rod (see Fig. 6). The length of the scans is 2.54 mm.

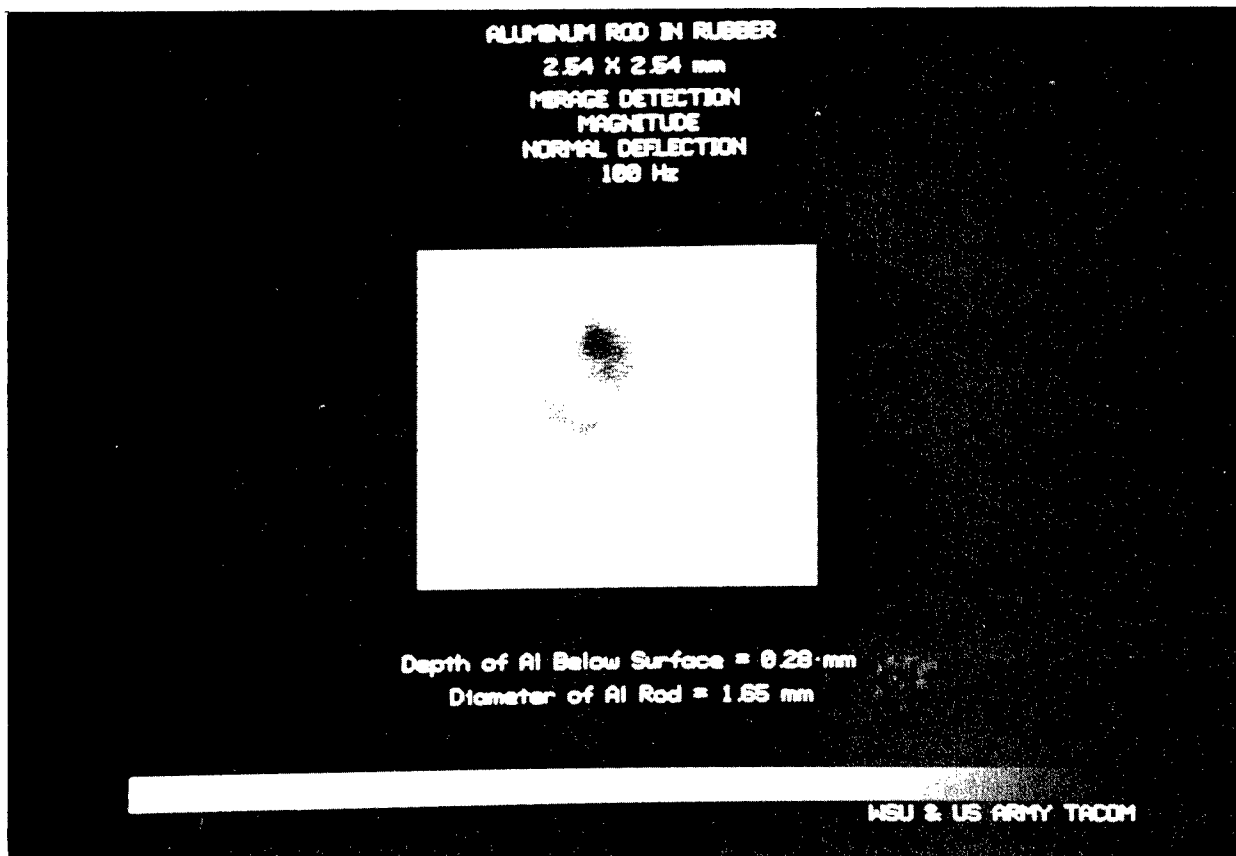


Fig. 11. Thermal wave MIRAGE effect image at a frequency of 100 Hz, using the normal deflection magnitude signal, of a 2.54 mm x 2.54 mm area of the surface of the Rubber ABR sample above the cylindrical hole filled with an aluminum rod (see Fig. 6).

3. 10 phr N326 poor dispersion  
(Sample 901-83B)
4. 10 phr Coarse Whiting (calcium carbonate) good dispersion  
(Sample 901-83E)
5. 10 phr Coarse Whiting poor dispersion  
(Sample 901-83D)

One side of each sample was cured against a smooth plate. Mr. Beatty reported that it was difficult to make a poor dispersion, even though N326 black was used (it is known to be somewhat more difficult to disperse than the high structure blacks). Additionally, he reports that the whiting or calcium carbonate is the coarsest pigment grade used in the rubber industry.

### 2.5. Thermal Wave Images of Good Dispersion and Poor Dispersion Rubber

The thermal wave images shown in Figures 12 - 16 were obtained by monitoring the magnitude of the normal deflection MIRAGE signal for each of the five rubber samples which were supplied. For each sample, images are shown for two modulation frequencies (400 Hz and 1 kHz). A scanned optical reflectivity image of the identical region is also included for each sample.

## 3.0. STUDIES OF CERAMIC-COATED SAMPLES

### 3.1. Thermal Wave Images of Ceramic-Coated SiC-6

Specimens of ceramic-coated (chemical vapor deposited [CVD] SiC) samples were provided by TACOM to test the ability of thermal wave imaging to assess coating thickness. The samples were fabricated by San Fernando Laboratories, 10258 Norris Ave., Pacoima, CA 91331. Thermal wave MIRAGE (magnitude of the normal deflection) images, together with corresponding scanned optical images of five different regions of Sample 1-ND (a CVD SiC coating 0.003" thick on a substrate of SiC-6, which is a graphite with a coefficient of thermal expansion matched to SiC, are shown in Fig. 17. The signal-to-noise ratio is good, and the granularity of the coating is quite evident in these images. This granularity can be thought of as constituting an irreducible 'material noise' for such a sample, however, and may determine the lower size limit for defect detection.

### 3.2. Thermal Diffusivity Measurements of Ceramic-Coated SiC-6

On the basis of other measurements of coated materials<sup>14</sup>, we have determined the best thermal wave method for characterizing such coatings is one which is sensitive to lateral heat flow along the surface of the coating. In particular, the quantity we choose to measure is the in-phase transverse MIRAGE signal as a function of the transverse offset between the positions of the probe beam and the heating beam as the heating beam is scanned across the (fixed) probe beam.<sup>14</sup> Three such traces are shown

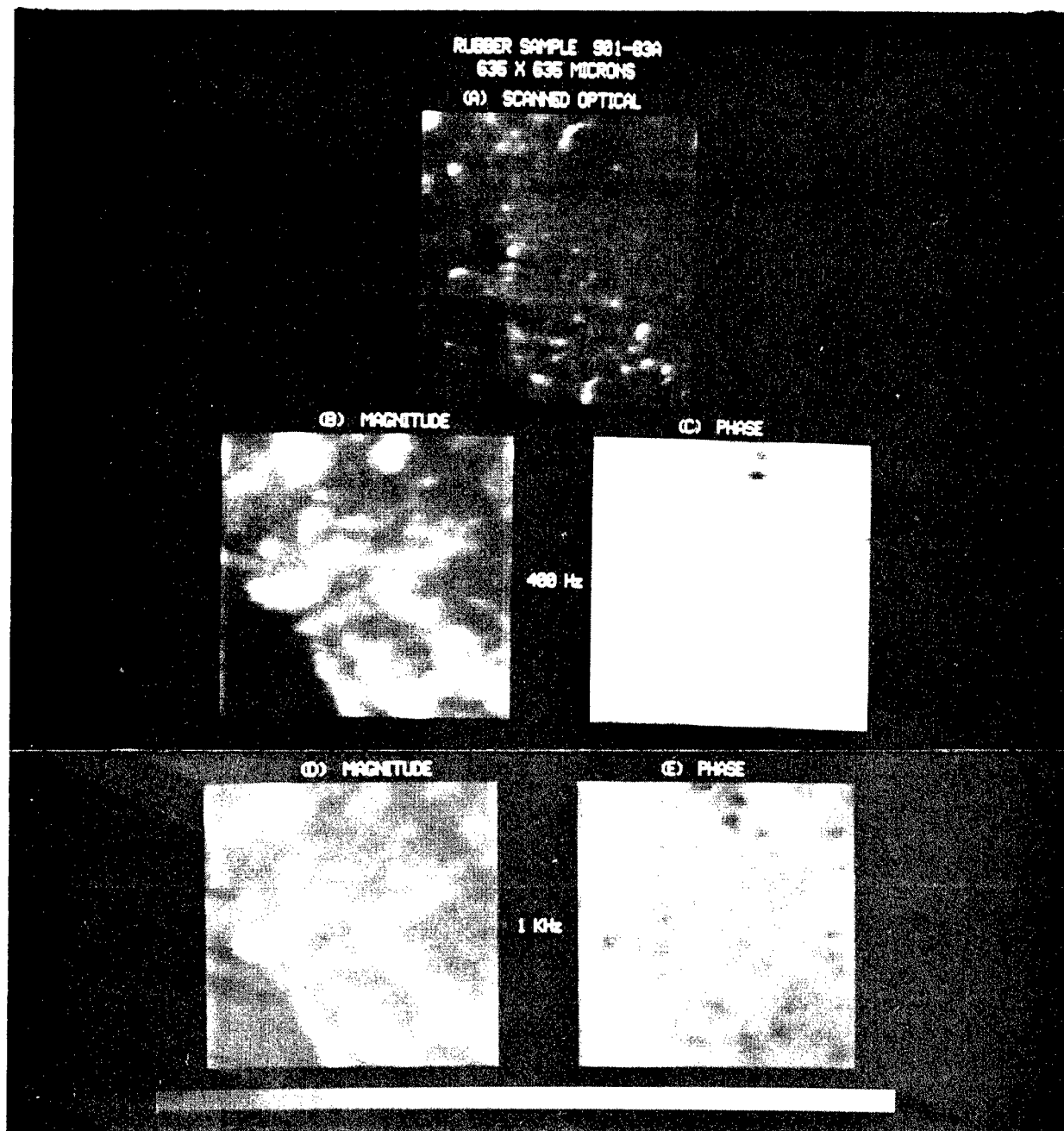


Fig. 12. Representative MIRAGE thermal wave and scanned optical images of Rubber Sample 901-83A (pure gum of peroxide and synthetic polyisoprene) [ a) 400 Hz scanned optical; b) 400 Hz MIRAGE magnitude; c) 400 Hz MIRAGE phase; d) 1 kHz MIRAGE magnitude; e) 1 kHz MIRAGE phase].

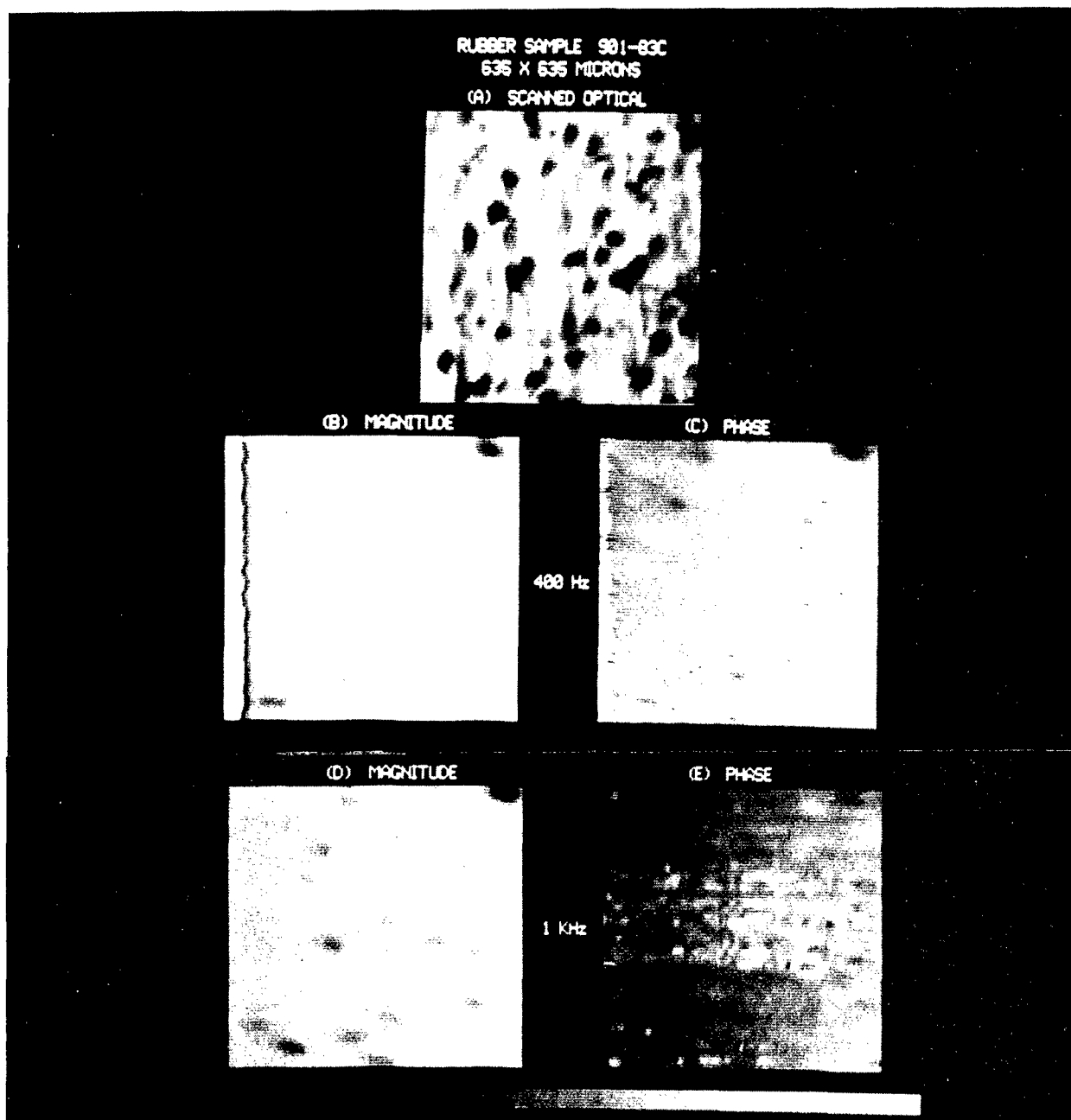


Fig. 13. Representative MIRAGE thermal wave and scanned optical images of Rubber Sample 901-83C (10 phr N326, low structure HAF, good dispersion) [ a) 400 Hz scanned optical; b) 400 Hz MIRAGE magnitude; c) 400 Hz MIRAGE phase; d) 1 kHz MIRAGE magnitude; e) 1 kHz MIRAGE phase]. The bright vertical bars in b) and c) are artifacts.

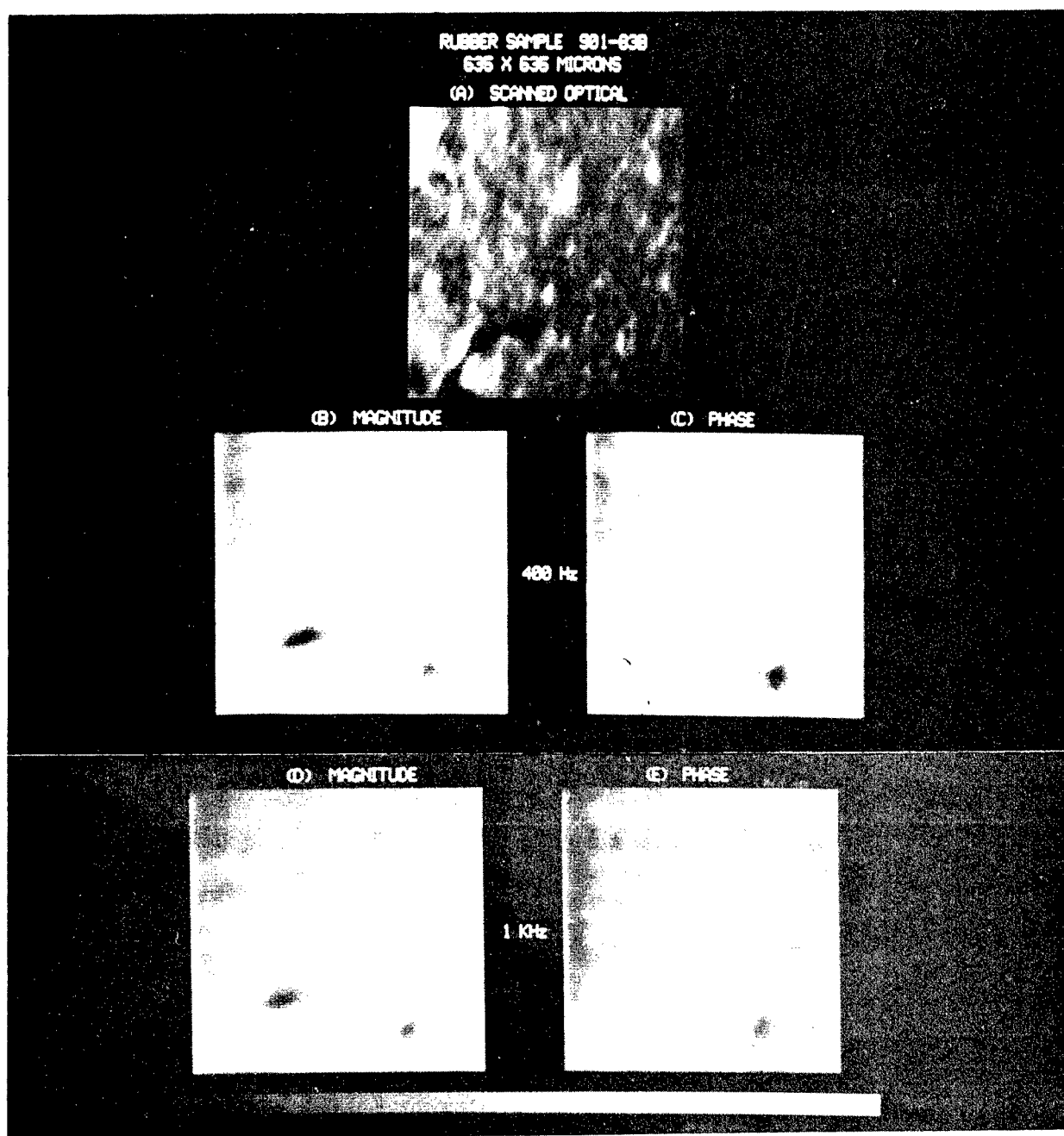


Fig. 14. Representative MIRAGE thermal wave and scanned optical images of Rubber Sample 901-83B (10 phr N326 poor dispersion). [ a) 400 Hz scanned optical; b) 400 Hz MIRAGE magnitude; c) 400 Hz MIRAGE phase; d) 1 kHz MIRAGE magnitude; e) 1 kHz MIRAGE phase].

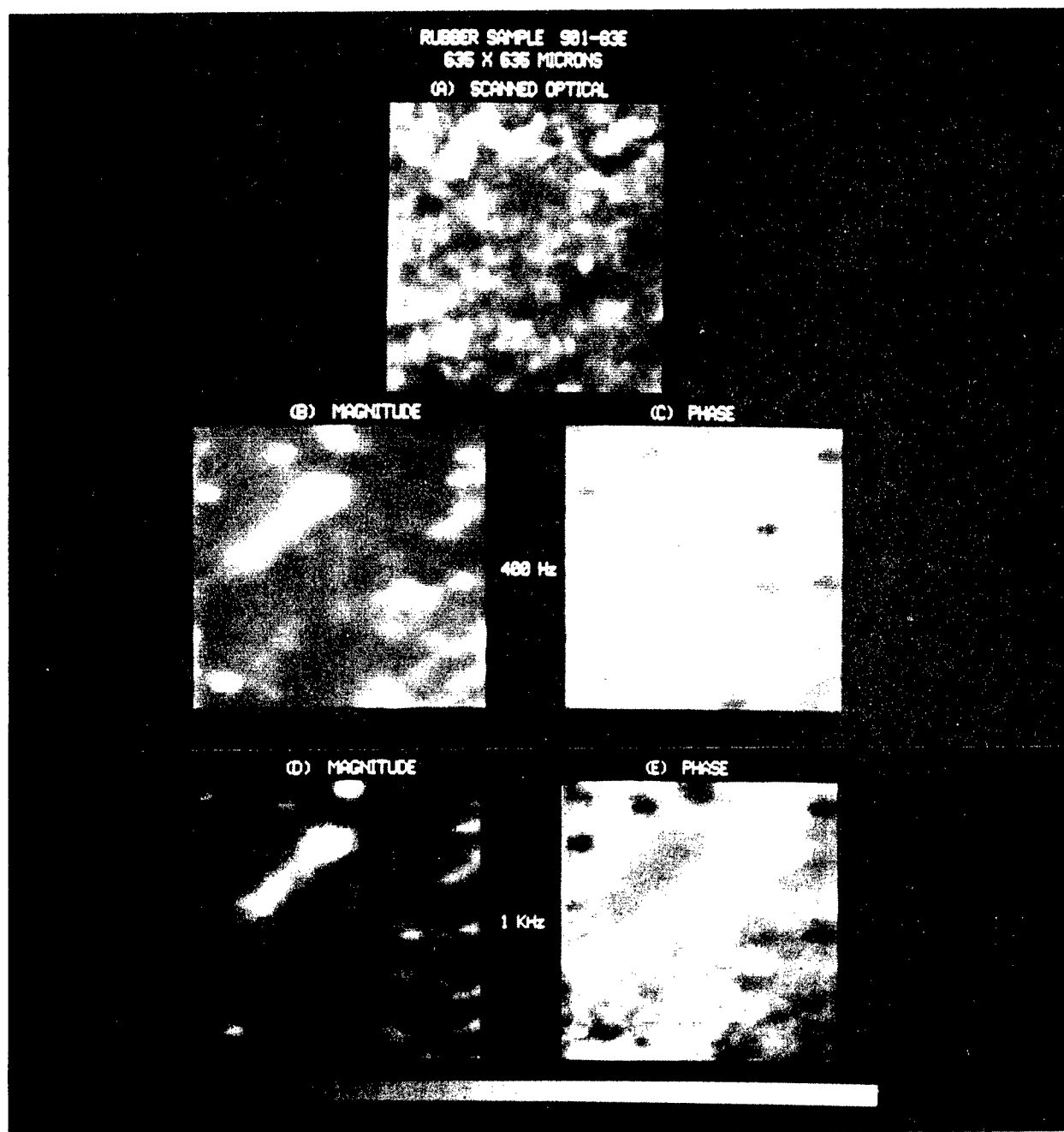


Fig. 15. Representative MIRAGE thermal wave and scanned optical images of Rubber Sample 901-83E (10 phr Coarse Whiting, calcium carbonate, good dispersion). [ a) 400 Hz scanned optical; b) 400 Hz MIRAGE magnitude; c) 400 Hz MIRAGE phase; d) 1 kHz MIRAGE magnitude; e) 1 kHz MIRAGE phase].

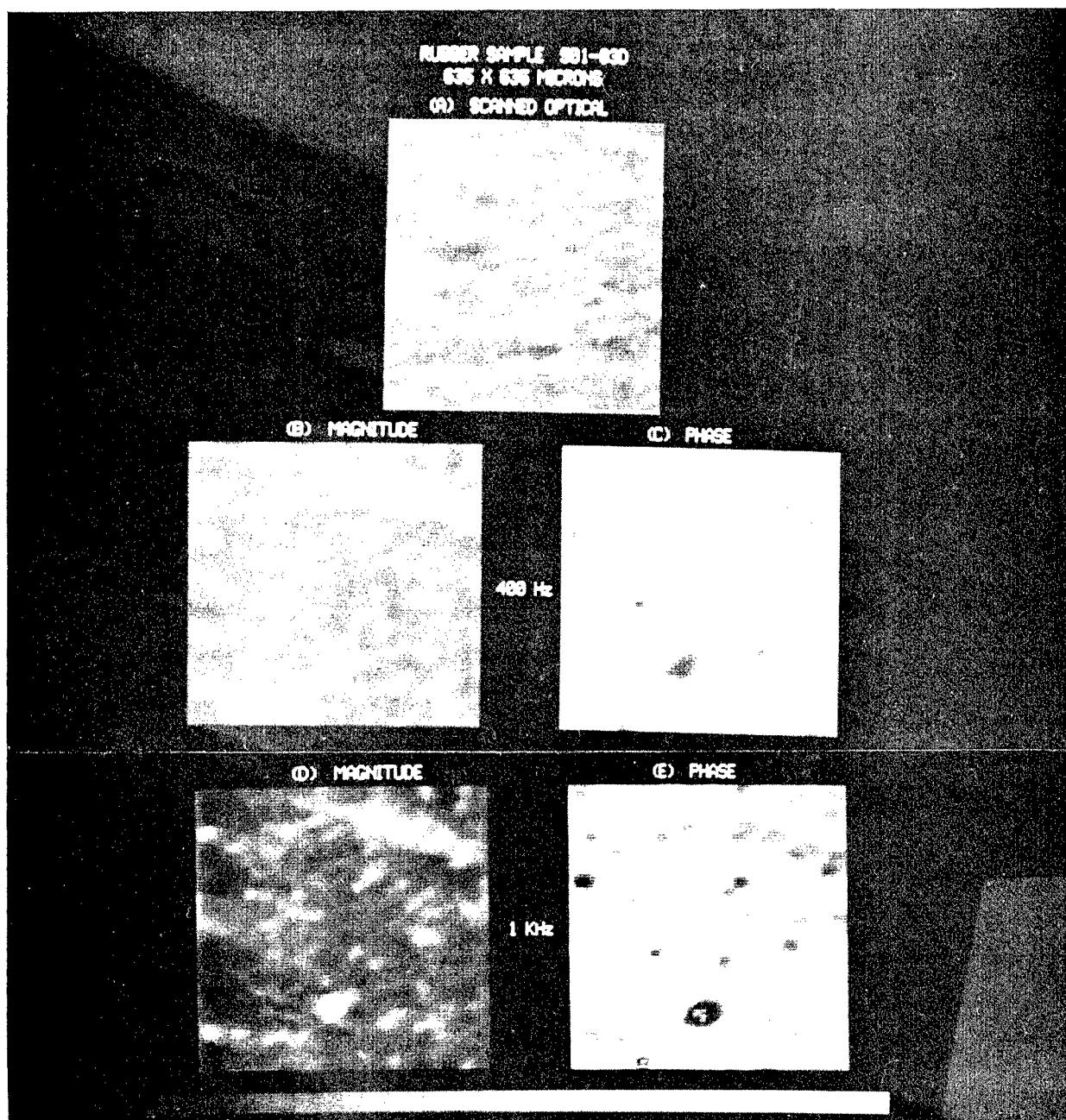


Fig. 16. Representative MIRAGE thermal wave and scanned optical images of Rubber Sample 901-83D (10 phr Coarse Whiting, poor dispersion [ a) 400 Hz scanned optical; b) 400 Hz MIRAGE magnitude; c) 400 Hz MIRAGE phase; d) 1 kHz MIRAGE magnitude; e) 1 kHz MIRAGE phase].



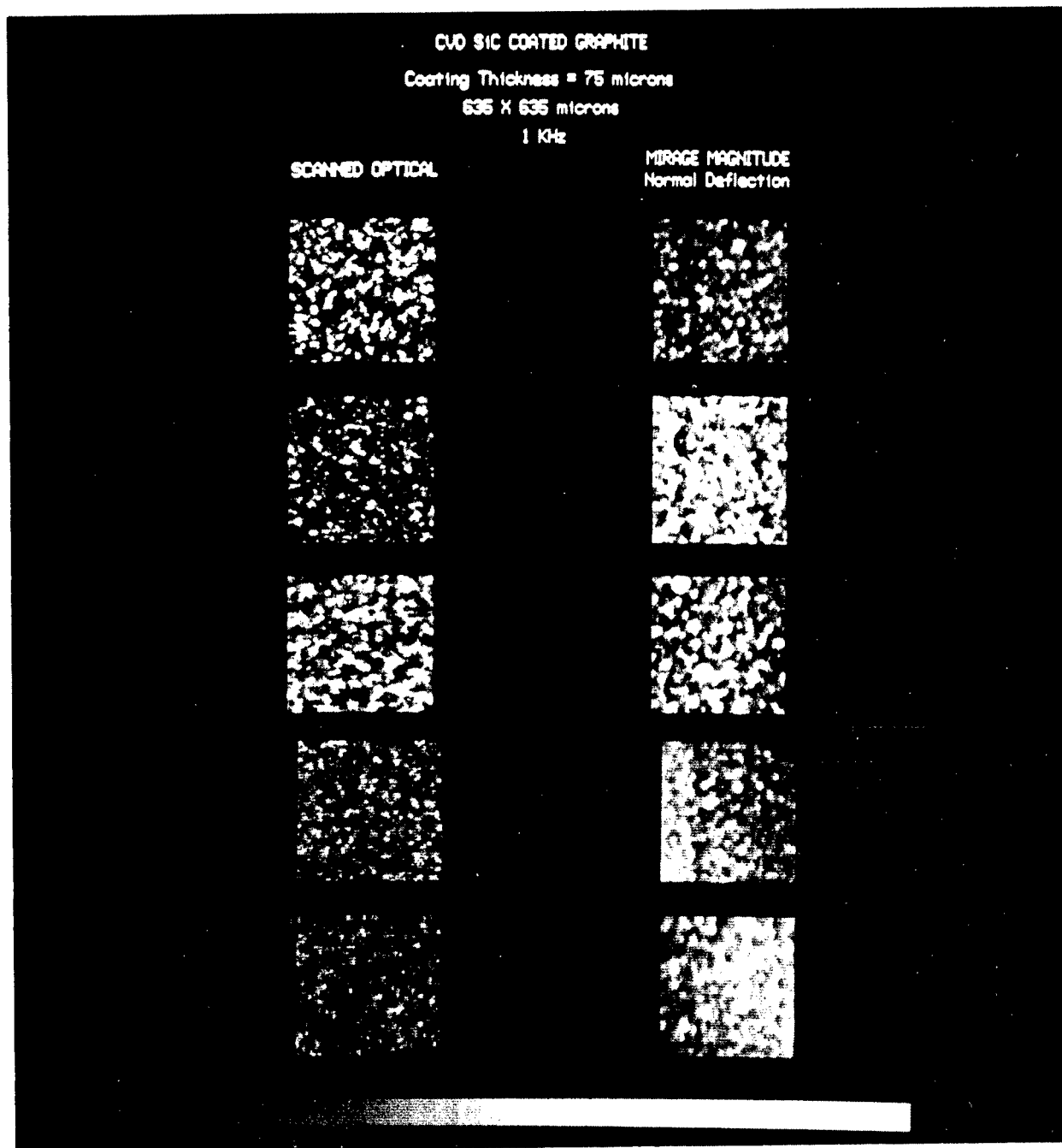


Fig. 17. Thermal wave MIRAGE thermal wave and scanned optical images of five different regions on the same ceramic-coated sample (Sample 1-ND, a CVD SiC coating 0.003" thick on a substrate of SiC-6).

in Fig. 18, for the case of InSb. The quantity,  $x$ , shown in Fig. 18, is the easily determined separation between the closest noncentral zero-crossings of the signal, and is directly related to the thermal wavelength in the material. Plots of this quantity versus  $f^{-1/2}$  (see Fig. 19) directly yield the thermal diffusivity.<sup>14</sup> Furthermore, if one compares such plots between coated and uncoated regions of a 0.5 mil thick AEP 32 coating on a nickel-based (713C) alloy turbine blade<sup>14</sup> (Fig. 20), differences between the coated and uncoated regions are clearly evident. In Figs. 21-25, we present similar plots for a CVD SiC ceramic coating on a SiC-6 substrate, and for four different thicknesses of CVD SiC ceramic coatings on ZrO<sub>2</sub> substrates. Comparing Figs. 21-25 shows that the slope of the plots at low frequencies is determined by the thermal diffusivity of the substrate.

#### 4.0. IMAGING OF HOLLOW TURBINE BLADES

Recently,<sup>13</sup> several of us have carried out resolution studies of thermal wave imaging, including a series of experimental and theoretical investigations of thermal wave scattering from subsurface "targets". Targets of rectangular, spherical, and cylindrical geometry were considered for different depths (as a fraction of the thermal wavelength). Of particular relevance to the problem under consideration here, namely a cooling passage in a metal turbine blade, are the partial wave expansion calculations for the case of a cylindrical target of relatively poor thermal conductivity (air), and the confirming experimental results. The results of these calculations and experiments are summarized in Figs. 26 and 27, respectively. The experiments were carried out using the normal deflection MIRAGE technique with the probe beam perpendicular to the direction of the channel. The frequency dependences of both the magnitude and the phase of the signal are in good agreement with the theoretical predictions. This was also found to be the case for thermal wave scattering from a subsurface cylinder of relatively high thermal diffusivity as well as for spherical subsurface objects.

The results of the studies described above for simple geometries, and in particular for a subsurface cylindrical air hole parallel to the top surface of a metal, are now applied to a practical problem. In Fig. 28, we present the results of similar measurements on a section of a TF30 first stage turbine blade, thermally imaging two cooling air holes at the trailing edge of the blade. The MIRAGE (magnitude of the normal deflection) technique was used, at a frequency of 5.4 Hz, in order to detect the holes, which are thermally quite deep (compare Figs. 26 and 27 above). The cooling holes are indeed detectable, although the signal is most sensitive to the section of the cylindrical boundary which is closest to the top surface. This signal decreases rapidly in strength for scattering from deeper sections of the surface.

We also scanned sections of the surface of this blade for which previous radiographic studies had indicated the possible presence of subsurface defects. The results of such a scan are shown in Fig. 29.

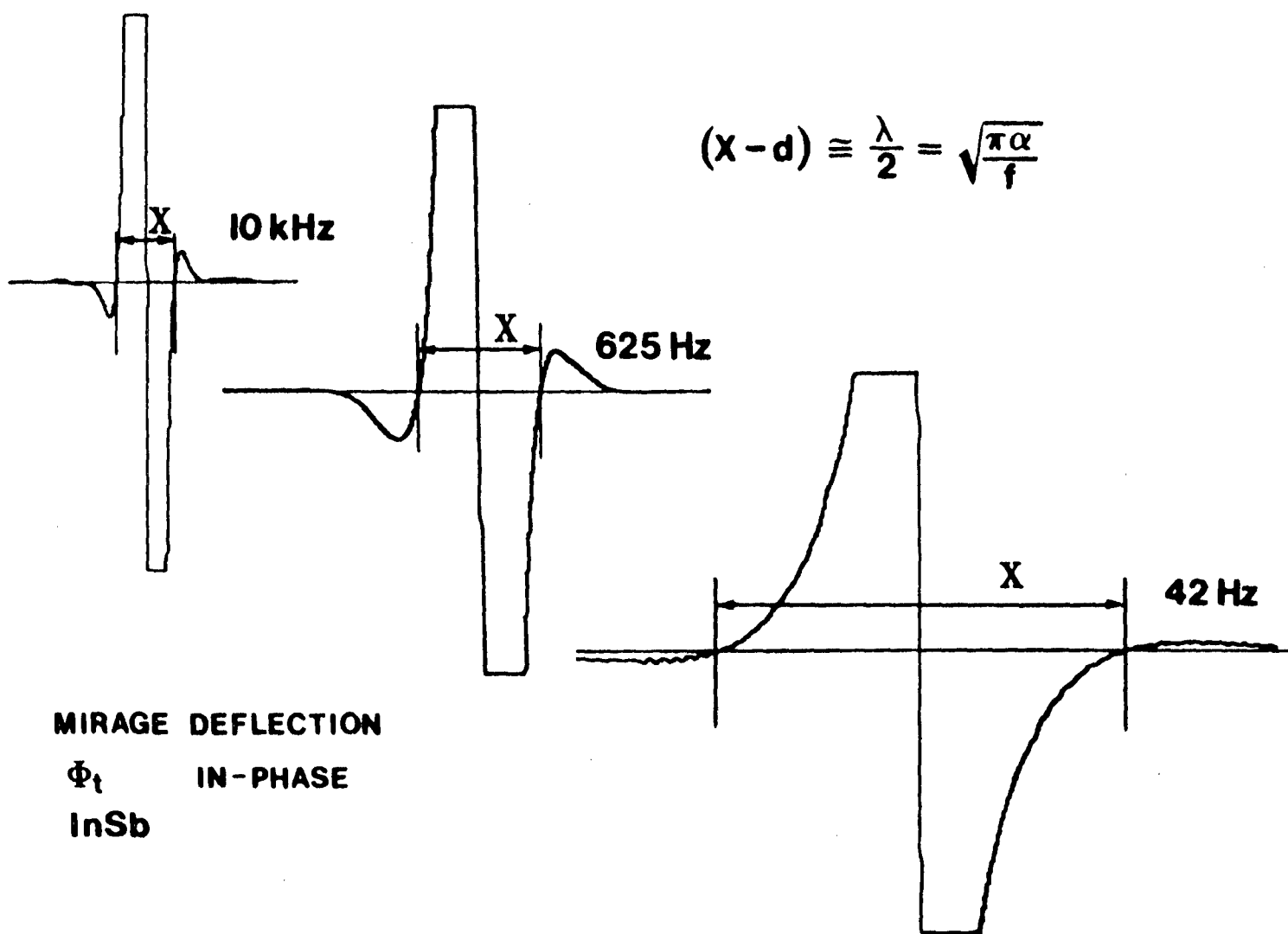


Fig. 18. Line traces showing the frequency dependence of the zero crossings (x) for the in-phase component of the transverse MIRAGE deflection for a single crystal of InSb.

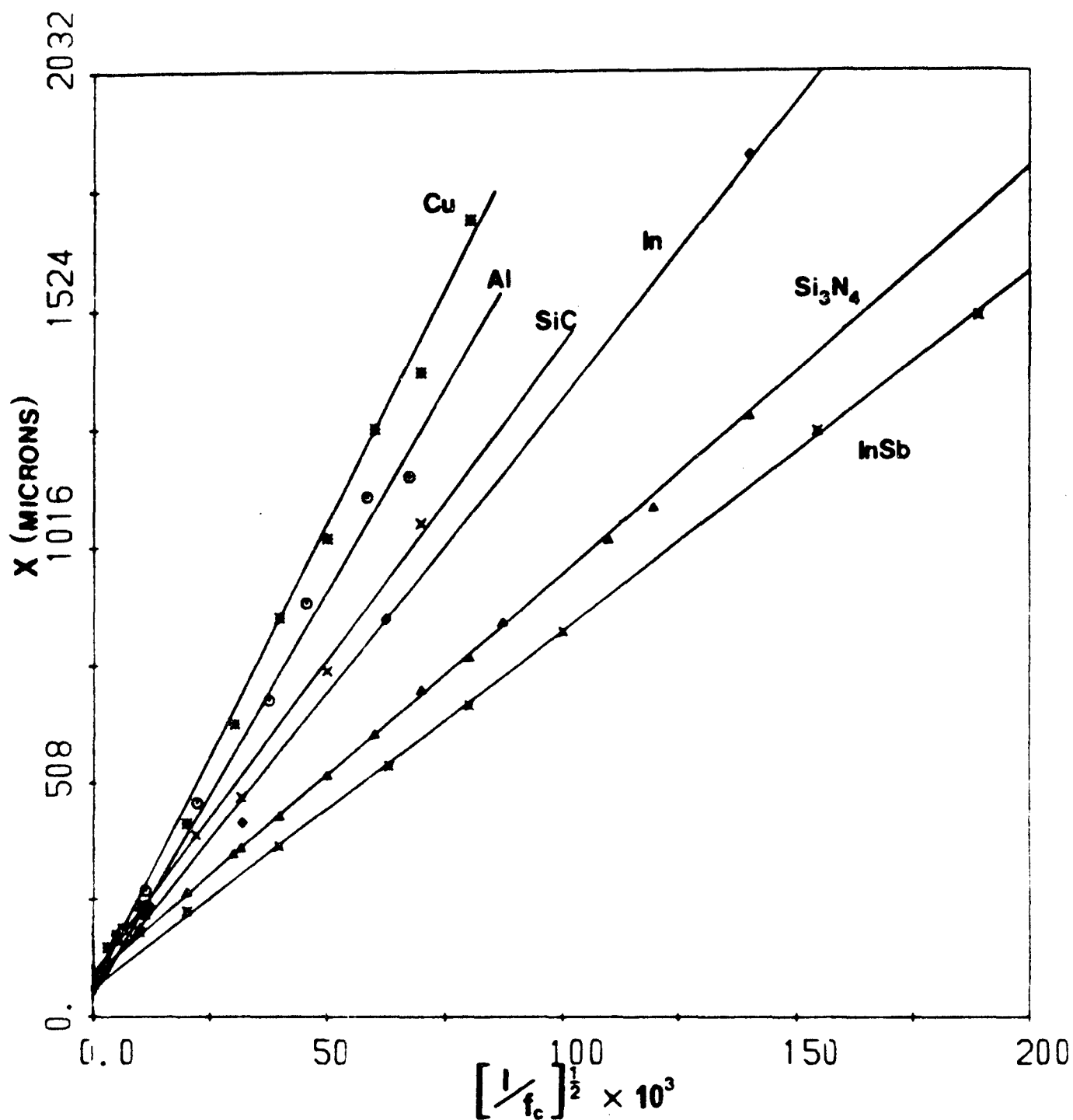


Fig. 19. A graph of the measured zero crossings (x) for Cu, Al, SiC, In,  $Si_3N_4$ , and InSb, plotted as a function of inverse-square-root frequency. The measured slopes give values for the thermal diffusivities of these materials that are in good agreement with those found in the literature.

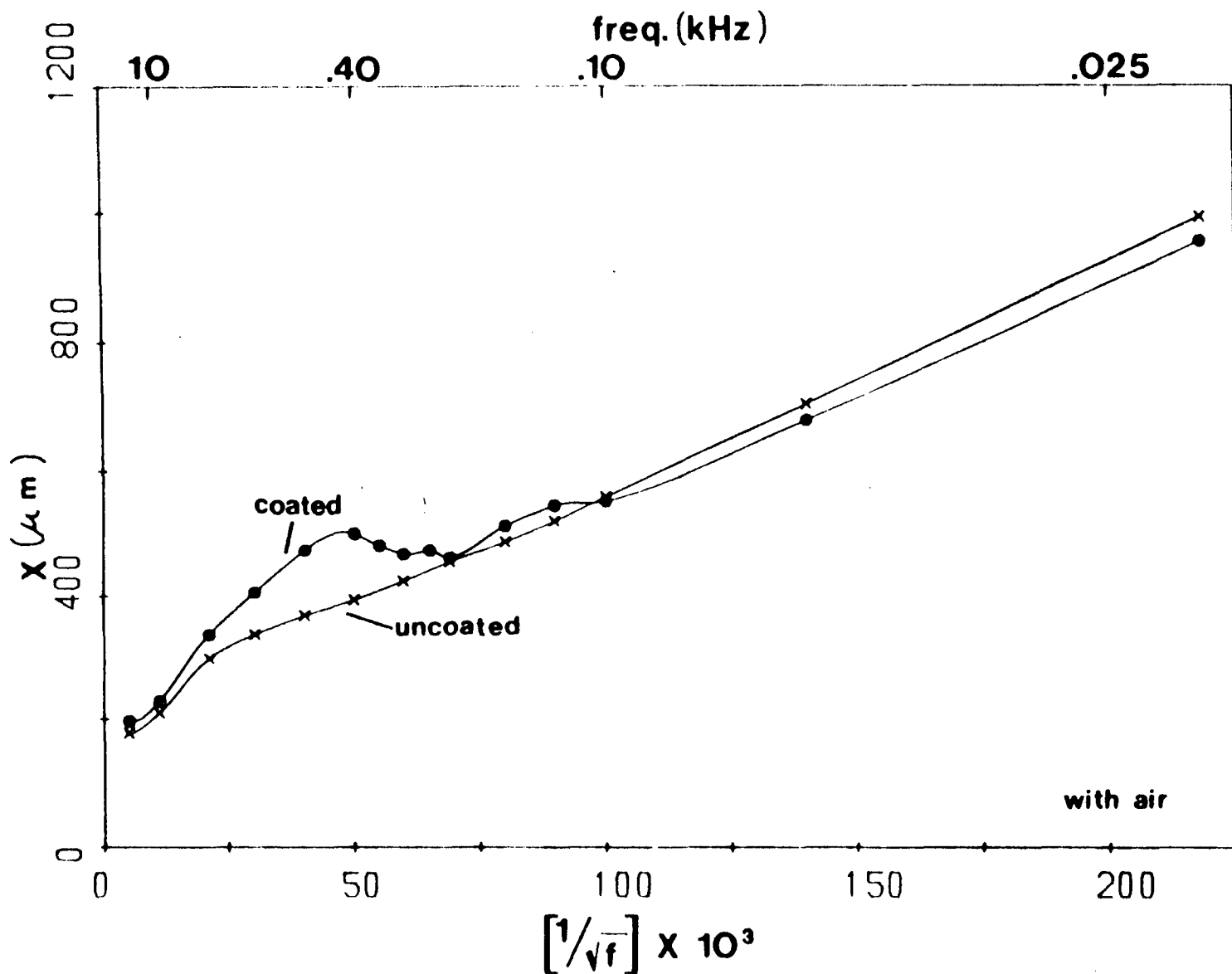


Fig. 20. A graph of the measured zero crossings (x) for a coated nickel-based super-alloy (IN 738) plotted as a function of inverse-square-root frequency, for both the coated and uncoated portions of the sample.

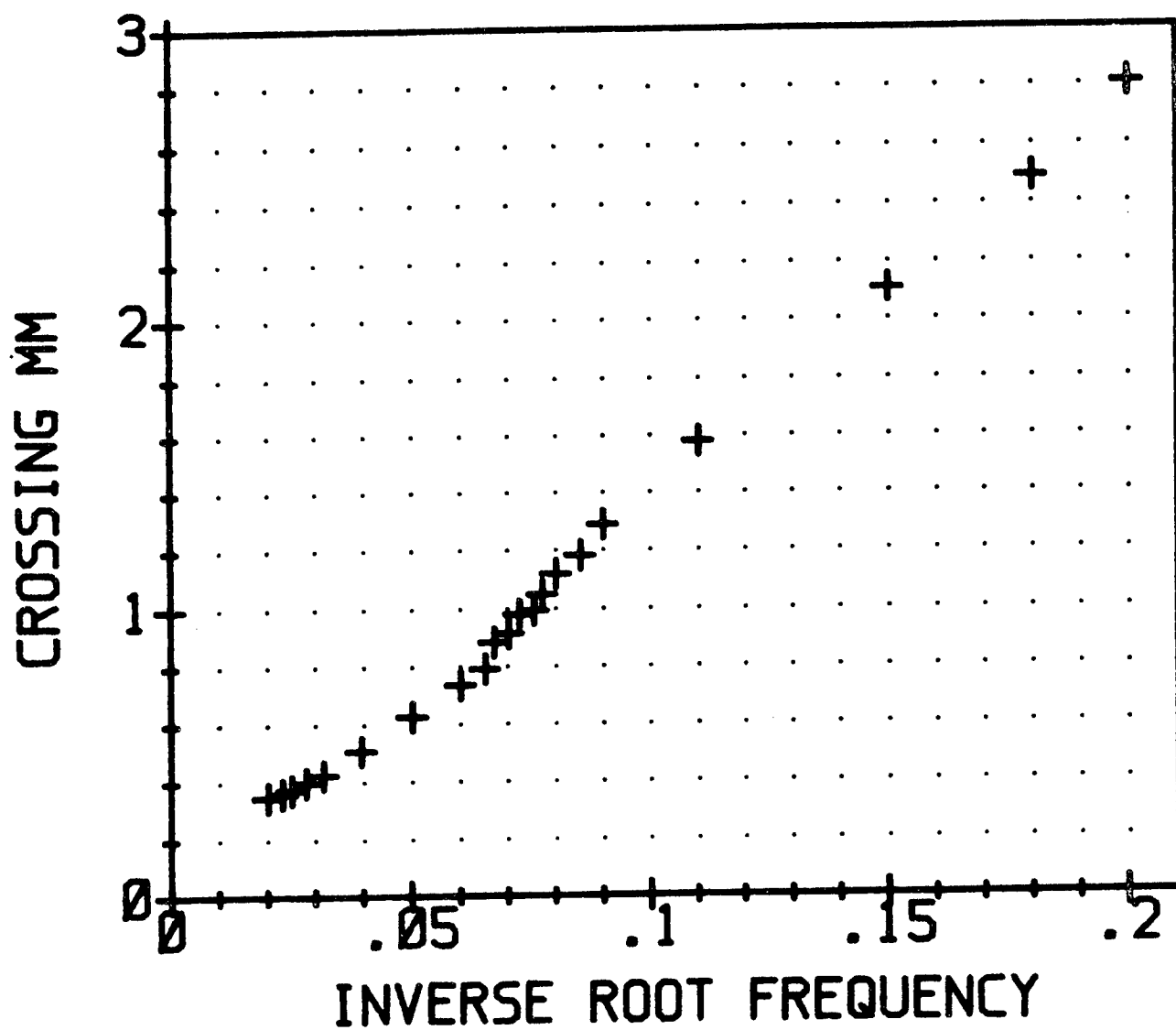


Fig. 21. A graph of the measured zero crossings (x) for ceramic-coated sample 1-ND (0.0033" coating of CVD SiC on a SiC-6 substrate).

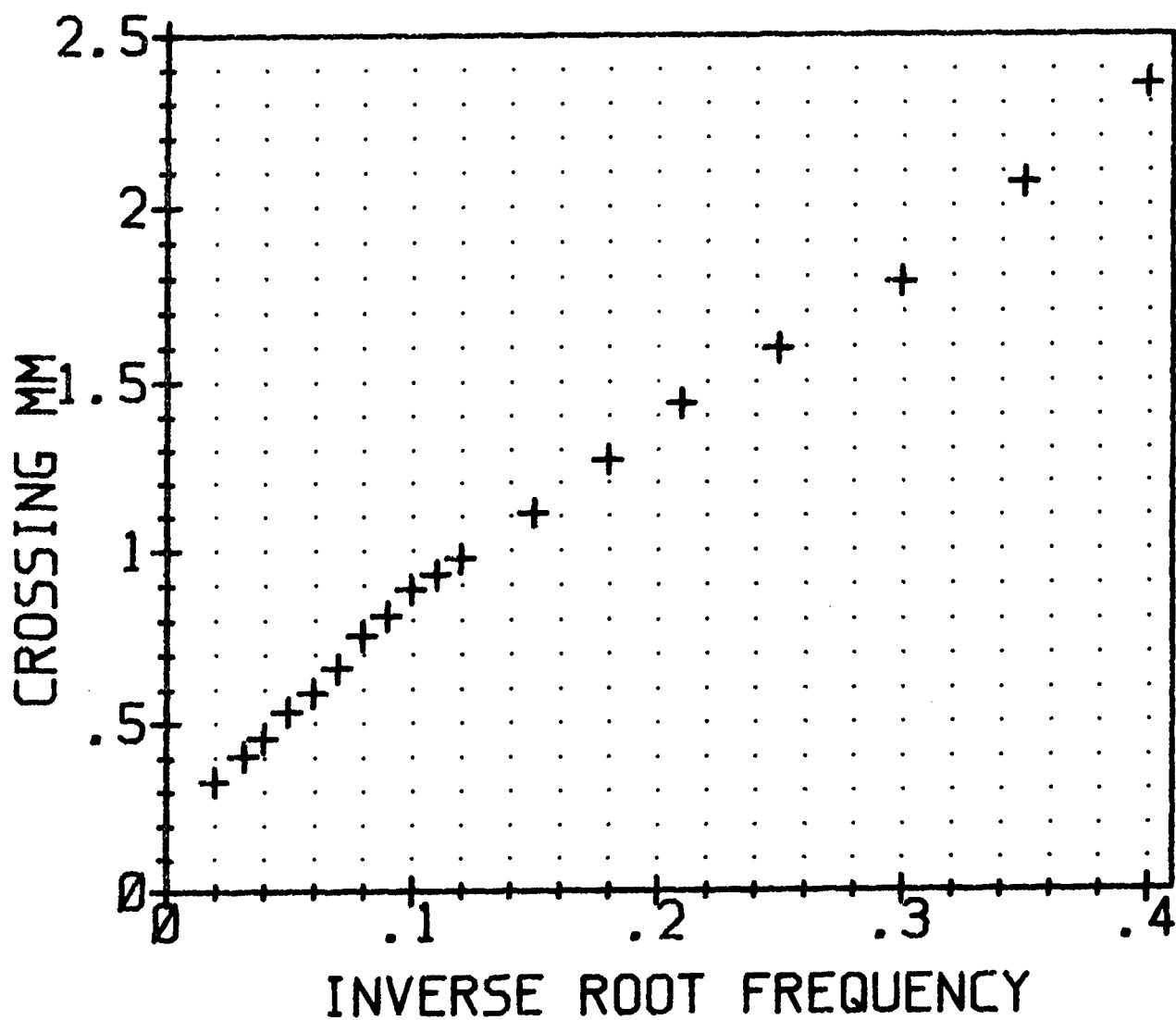


Fig. 22. A graph of the measured zero crossings (x) for ceramic-coated sample 1-ND (0.0033" coating of CVD SiC on a  $\text{ZrO}_2$  substrate).

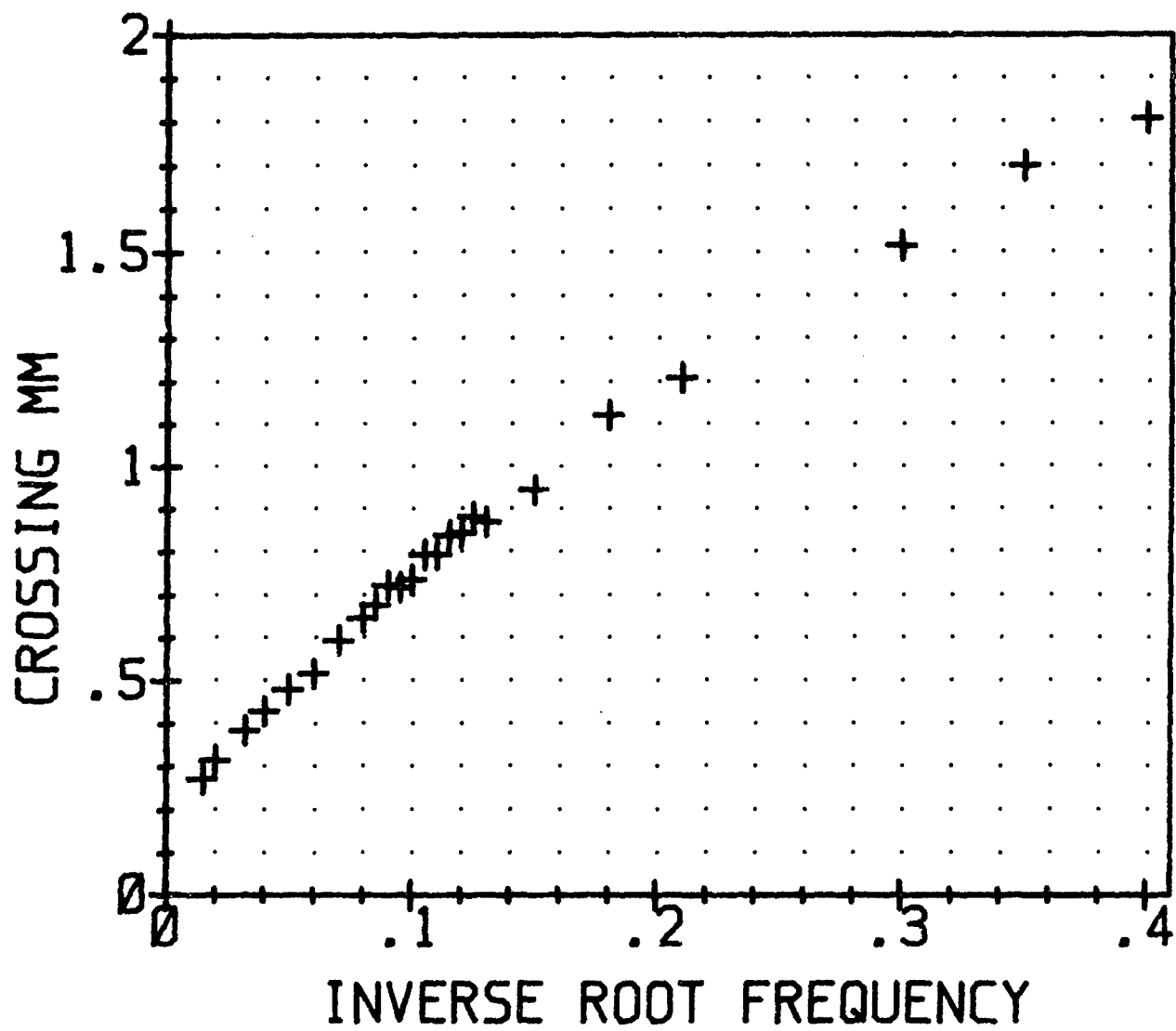


Fig. 23. A graph of the measured zero crossings (x) for ceramic-coated sample 2-A (0.0058" coating of CVD SiC on a  $\text{ZrO}_2$  substrate).



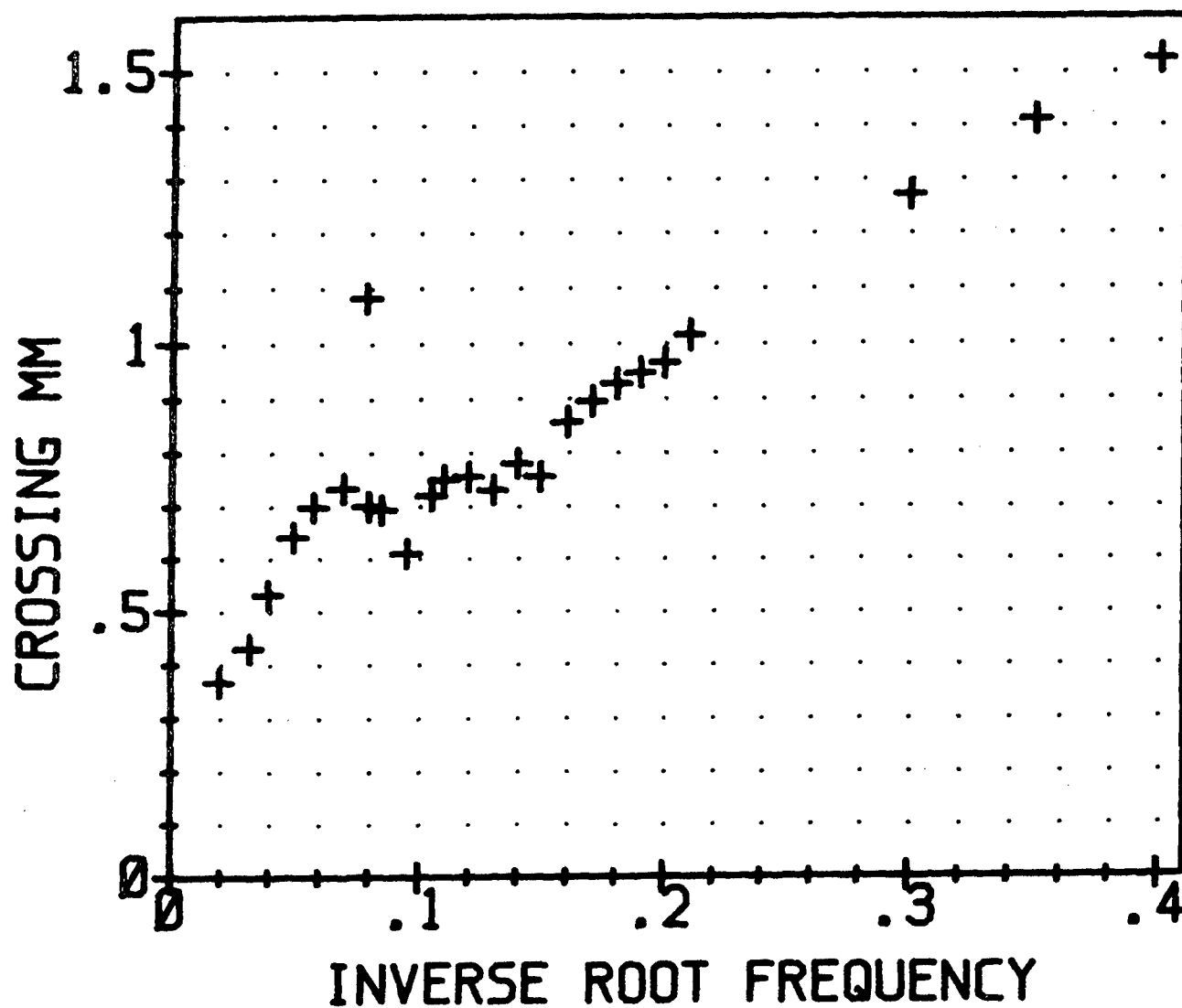


Fig. 24. A graph of the measured zero crossings (x) for ceramic-coated sample 3-B (0.007" coating of CVD SiC on a  $ZrO_2$  substrate).

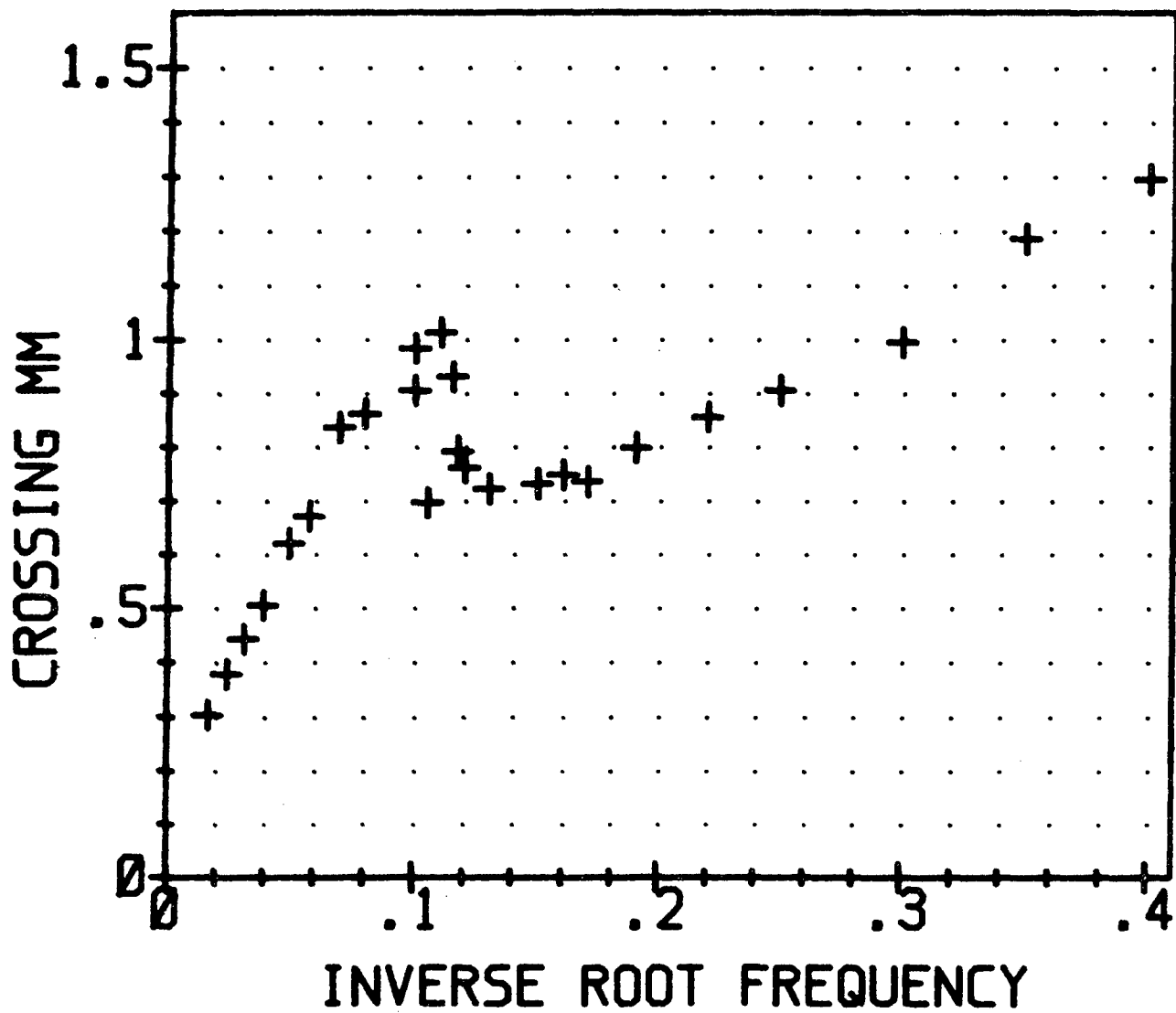


Fig. 25. A graph of the measured zero crossings (x) for ceramic-coated sample 1-A (0.0013" coating of CVD SiC on a  $\text{ZrO}_2$  substrate).

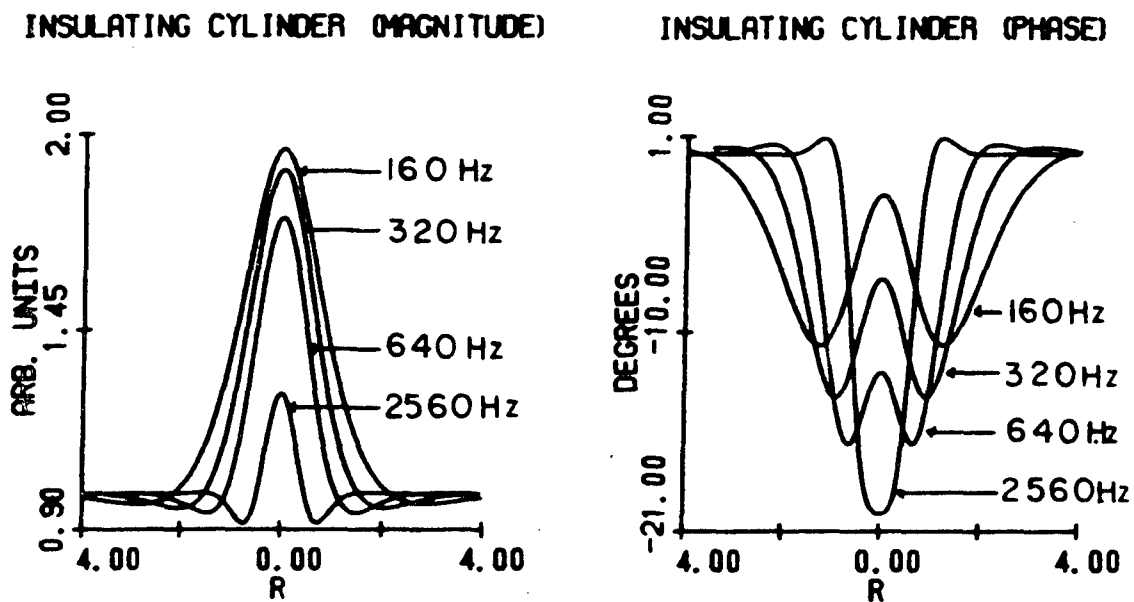


Fig. 26. Theory<sup>15</sup> for the thermal wave scattering from a subsurface cylinder of much lower thermal diffusivity than the host material.

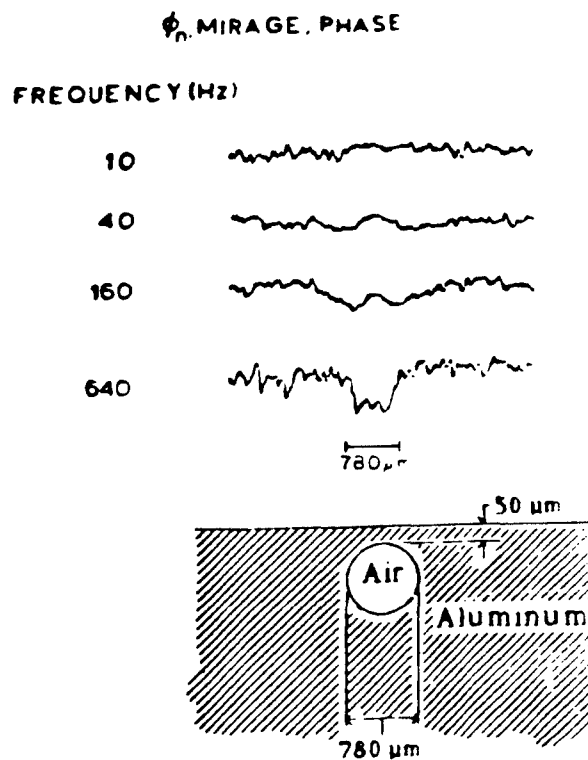
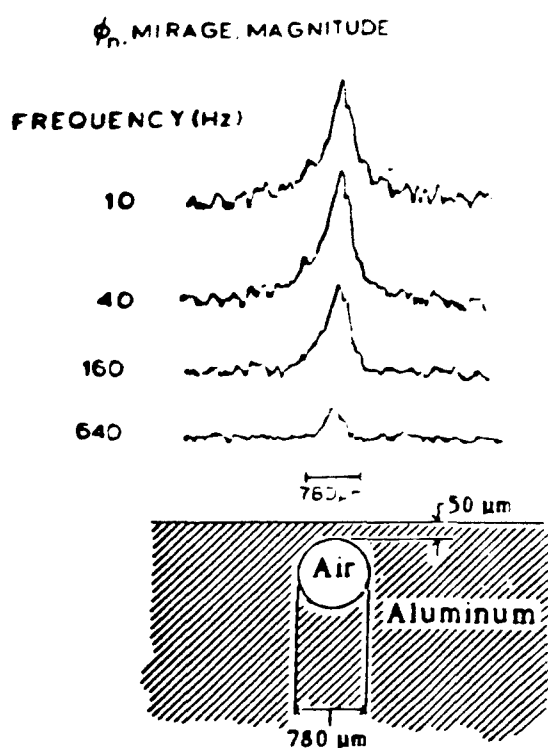


Fig. 27. Experimental results<sup>15</sup> for the thermal wave scattering from a subsurface cylinder of much lower thermal diffusivity than the host material.

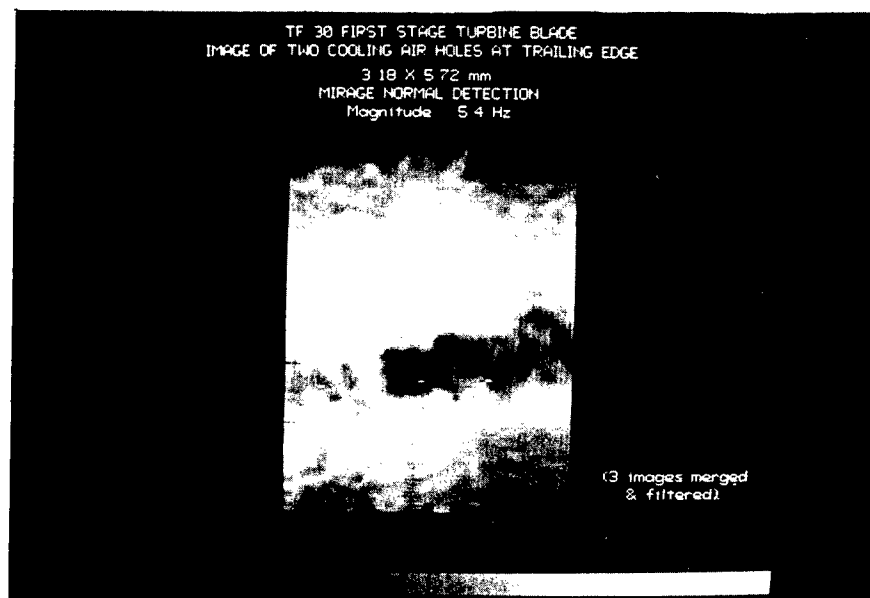


Fig. 28. Thermal wave MIRAGE (magnitude of the normal deflection) image of two cooling air holes at the trailing edge of a TF30 first stage turbine blade at a frequency of 5.4 Hz (compare with Figs. 26 and 27 above).

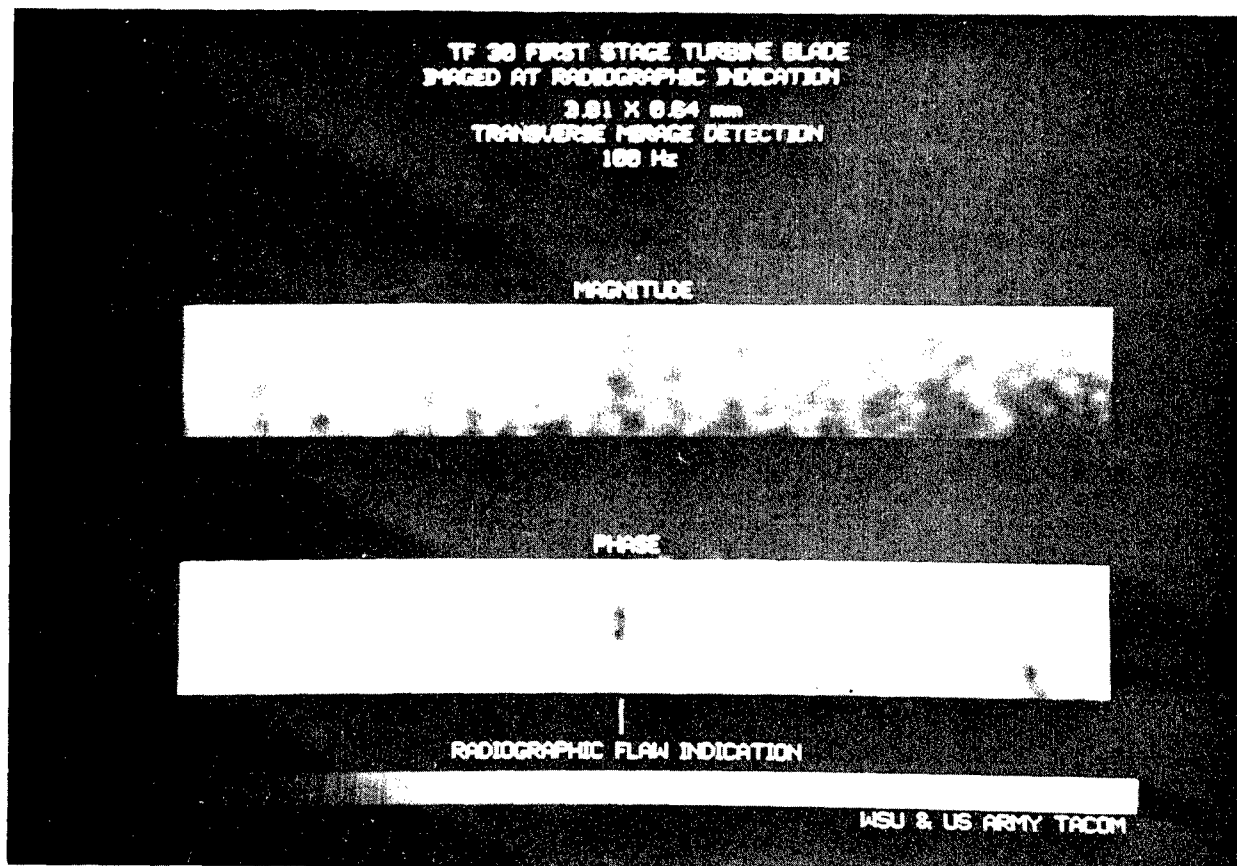


Fig. 29. Thermal wave MIRAGE (magnitude of the normal deflection at 100 Hz) image of a region of a TF30 first stage turbine blade for which previous radiographic studies had indicated the possible presence of subsurface defects.

## 5.0. MONOLITHIC $\text{Si}_3\text{N}_4$ AND SiC CERAMICS

### 5.1. Specimens.

The following monolithic  $\text{Si}_3\text{N}_4$  and SiC specimens were provided by Robert Brokelman of the Army Materials and Mechanics Research Center.:

Specimen No. 1 - Hot Pressed Silicon Nitride - NC132. One surface had been subjected to the following regular surface machining procedures: (a) rough grind with 120 grit wheel a total depth of 0.010". All grinding was parallel to the long axis of the sample with a removal rate of 0.0005" per pass; (b) finish grind with a 320 grit wheel an additional depth of 0.002". All grinding was parallel to the long axis of the sample with a removal rate of 0.0001" per pass. This procedure is considered to be a good machining practice for the AMMRC applications of this material, even though it can be expected to leave a network of cracks on the surface that extend about  $20 \times 10^{-6}$  meter (20 microns) deep. The other side of the specimen had a degraded surface produced by rough grinding at a much more severe removal rate as follows: (a) rough grind with a 120 grit wheel a total depth of 0.010". All grinding was parallel to the long axis of the sample with a removal rate of 0.003" per pass; (b) finish grind with a 320 grit wheel an additional depth of 0.002". All grinding was parallel to the long axis of the sample with a removal rate of 0.0001" per pass. A crack network considerably deeper than that produced by the regular surface machining procedure should result. However, since both surfaces were finish ground the same, they should look identical in a visual or microscopic examination.

Specimen No. 2 - Hot Pressed Silicon Carbide. This specimen was subjected to the same machining operations as Specimen No. 1.

Specimen No. 3 - Hot Pressed Silicon Nitride - NC132. This specimen was machined according to the regular procedure and then subjected to a temperature of 1200°C for 24 hours in air. This exposure usually causes a 25-50 reduction of strength. The mechanism of degradation is the formation of surface pits (roughly spherical) approximately 75 microns in diameter and one millimeter apart. The entire surface is sealed with an oxide layer ( $\text{SiO}_2$ ) which obscures the observations of such pits.

Specimen No. 4 - Hot Pressed Silicon Nitride - NC132. This specimen contains a row of three Knoop hardness machine-induced cracks on each large surface. The Knoop hardness indentations have been subsequently removed by machining, leaving semielliptical cracks on the surface. One surface contains cracks induced with a 2.7 kilogram Knoop load. The cracks are approximately 140 microns long by 70 microns deep on this surface. On the other side, a 1.7 kilogram load was used to produce cracks 110 microns long by 50 microns deep.

Specimen No. 5 - Hot Pressed Silicon Carbide. This specimen also contains surface cracks produced by 2.7 kilogram and 1.7 kilogram Knoop loads. The 2.7 kilogram load generated cracks approximately 130 microns long by 70

microns deep on one surface. On the other surface, the 1.7 kilogram load produced cracks approximately 130 microns long by 50 microns deep.

## 5.2. Thermal Wave Images of Monolithic Ceramics.

Specimen No. 1 - Thermal wave images for the regularly machined surface (R) and the degraded surface (D), taken with the normal deflection MIRAGE technique, are shown in Figs. 30 and 31, together with the corresponding scanned optical reflectivity images. While the machining marks are evident, it is not immediately obvious how the data differ for the two machining processes.

Specimen No. 2 - Images similar to those taken for Specimen No. 1 were also taken for Specimen No. 2, and are shown in Figs. 32 and 33. The conclusions are the same for this silicon carbide specimen as they were for the silicon nitride material.

Specimen No. 3 - A thermal wave (normal deflection magnitude MIRAGE technique) image and the corresponding scanned optical image for this heat-treated specimen are shown in Fig. 34. There are a number of more or less circular defects evident in the thermal wave image. Also, the sizes of these defects are close to the expected sizes of the surface pits, although their spacing is clearly much closer than the expected one millimeter (see Sec. 5.1). Also note that the thermal wave image is quite different from the scanned optical image of the identical region.

Specimen No. 4 - Since the cracks are expected to be nearly vertical, the thermal wave method of choice is the transverse deflection MIRAGE technique. Corresponding thermal wave and scanned optical images of both surfaces in the vicinities of one of the larger cracks and one of the smaller cracks are shown in Fig. 34. A comparison between the thermally deduced crack length and the nominal optical length (see Sec. 5.1) is given in Table 1. At this time, the theory is not sufficiently well developed to deduce the depth of the crack from the frequency dependence of the thermal wave signal, however, these same cracks were not observed by other NDE techniques.

Specimen No. 5 - Images similar to those described above for Specimen No. 4 are shown for Specimen No. 5 in Fig. 36.

## 6.0. RECOMMENDATIONS

### 6.1. Intrinsic Rubber Structure.

We have demonstrated that thermal wave imaging is capable of detecting subsurface structure. It is not obvious how these images correlate with the mechanical properties of interest. Furthermore, special care must be taken to insure that the thermal measurements are nondestructive. We have seen that the thermal diffusivity of rubber is poor, thereby limiting the depth (or equivalently, restricting the modulation frequencies to very low



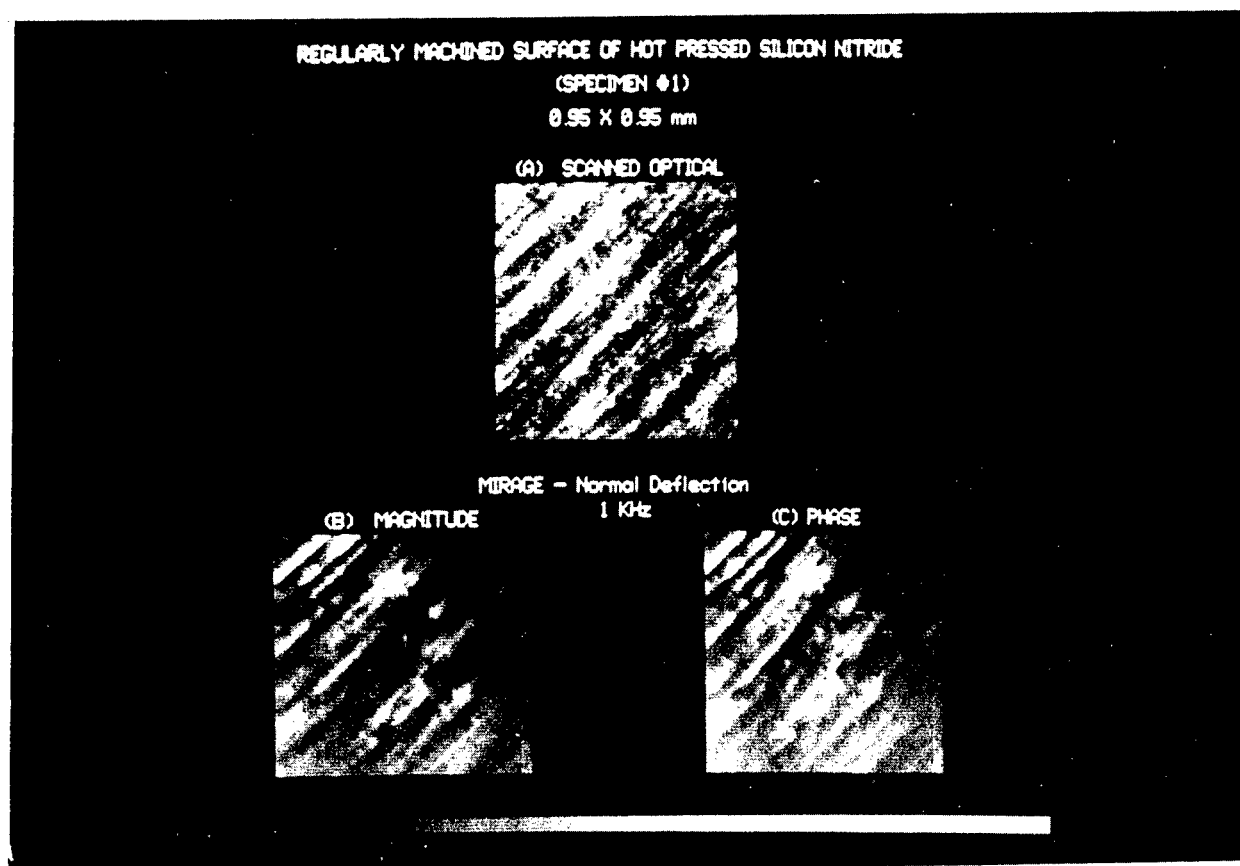


Fig. 30. Thermal wave MIRAGE (magnitude and phase of the normal deflection at 1 kHz) and scanned optical images for the regularly machined surface (R) of silicon nitride Specimen No. 1. [ a) optical; b) MIRAGE magnitude; c) MIRAGE phase ].

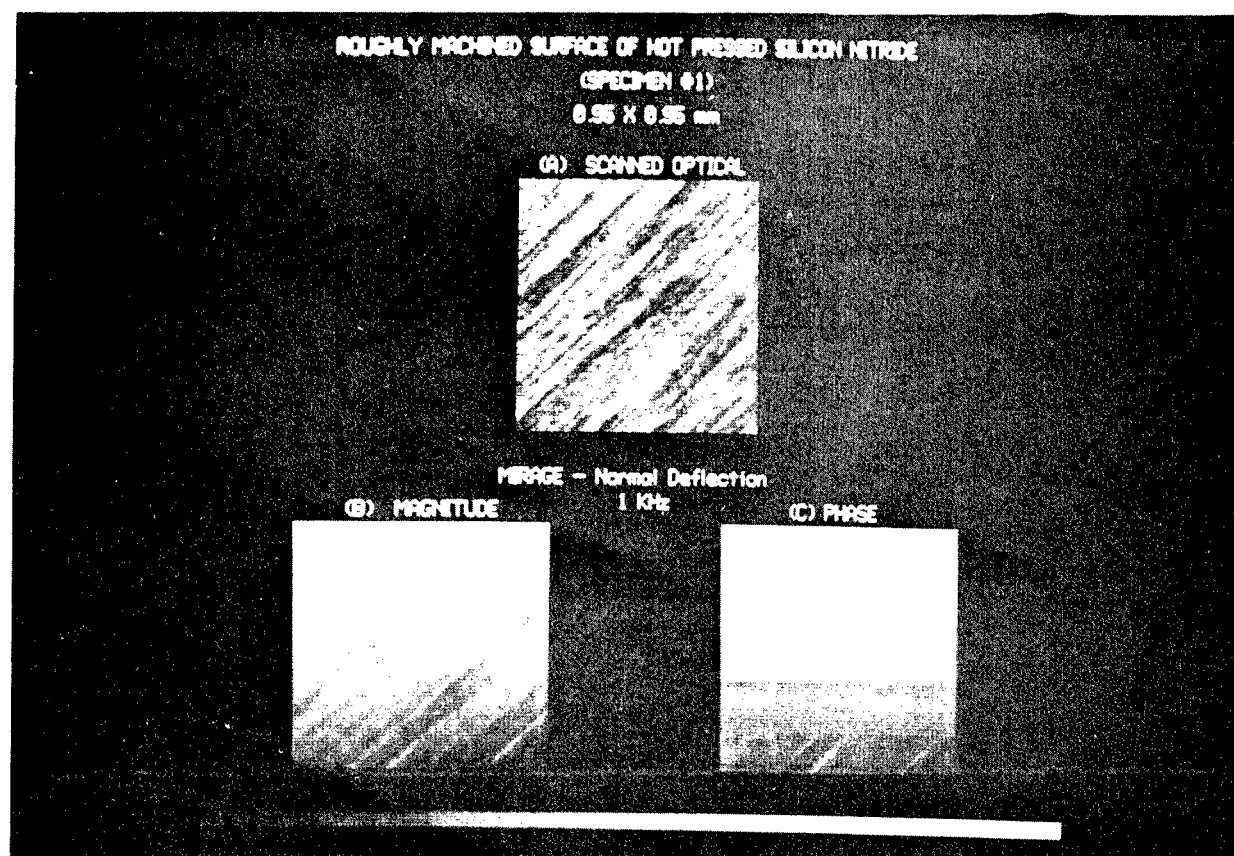


Fig. 31. Thermal wave MIRAGE (magnitude and phase of the normal deflection at 1 kHz) and scanned optical images for the degraded surface (D) of silicon nitride Specimen No. 1. [ a) optical; b) MIRAGE magnitude; c) MIRAGE phase ].

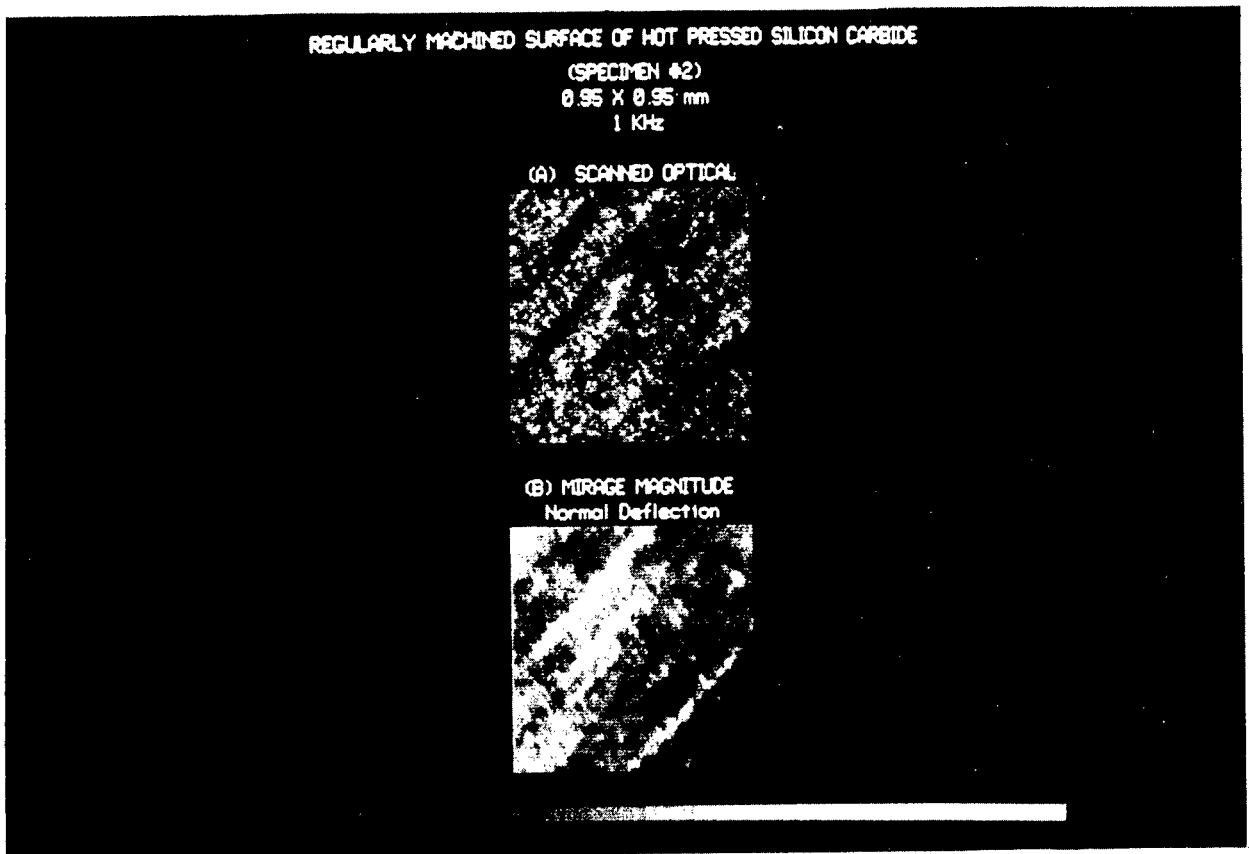


Fig. 32. Thermal wave MIRAGE (magnitude of the normal deflection at 1 kHz) and scanned optical images for the regularly machined surface (R) of silicon carbide Specimen No. 2. [a) optical; b) MIRAGE magnitude].

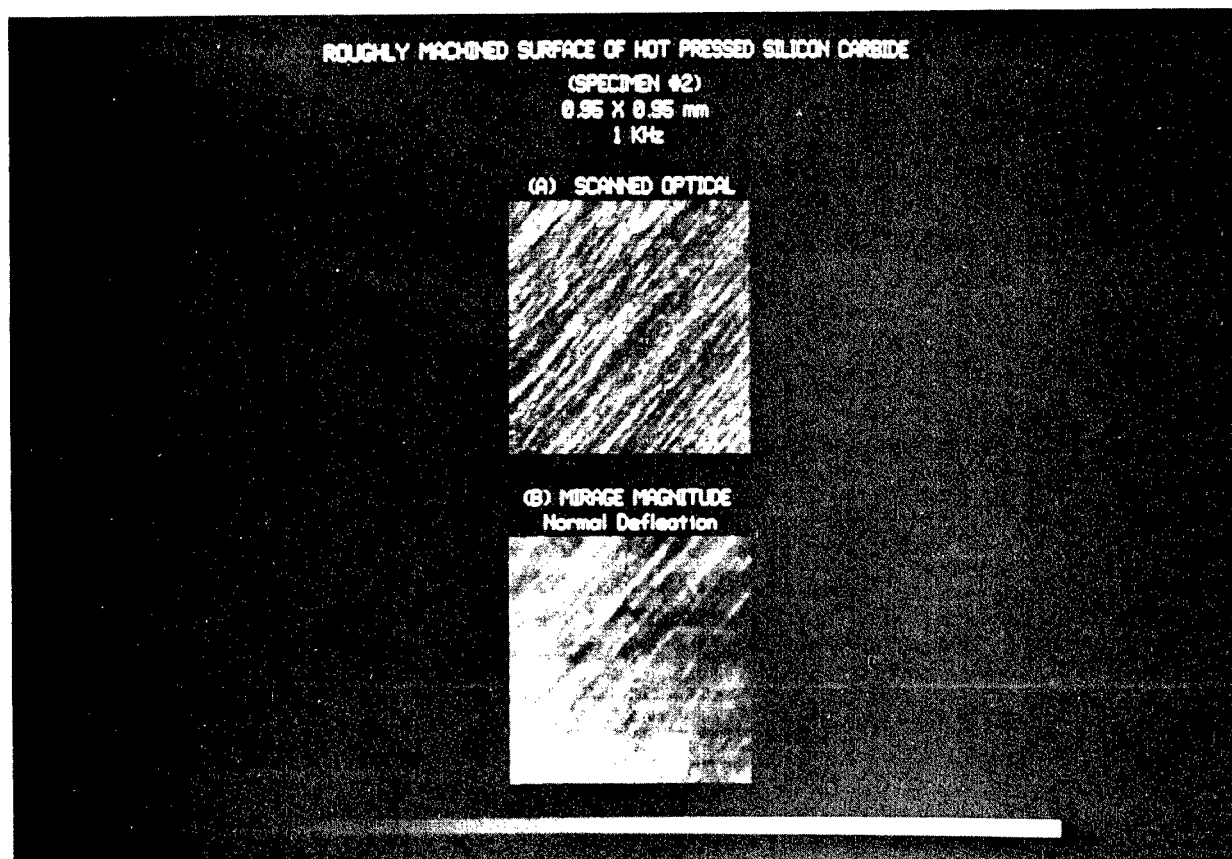
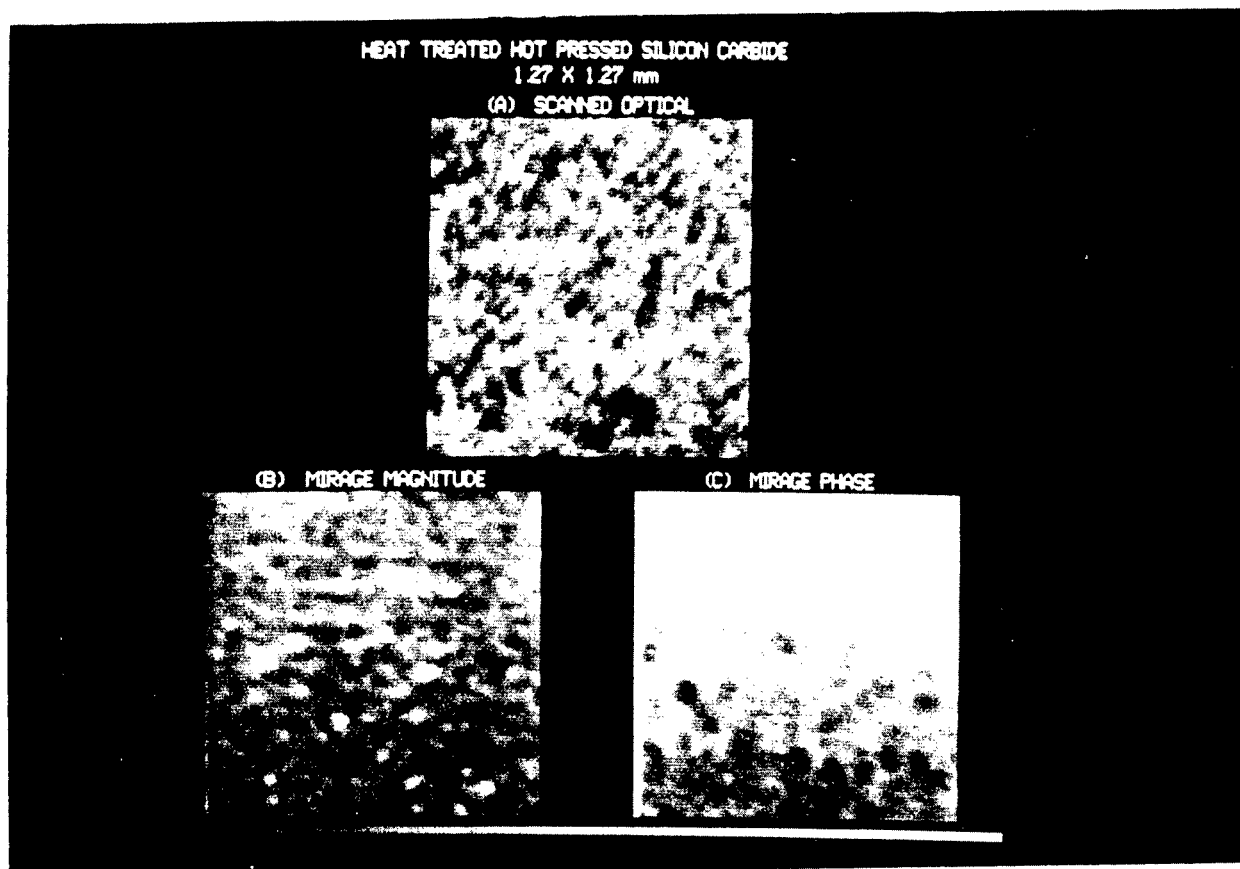


Fig. 33. Thermal wave MIRAGE (magnitude of the normal deflection at 1 kHz) and scanned optical images for the degraded surface (D) of silicon carbide Specimen No. 2. [ a) optical; b) MIRAGE magnitude ].



**Fig. 34.** Thermal wave MIRAGE (magnitude and phase of the normal deflection at 1 kHz) and scanned optical images for the heat-treated specimen of silicon carbide (Specimen No. 3). [ a) optical; b) MIRAGE magnitude; c) MIRAGE phase ].

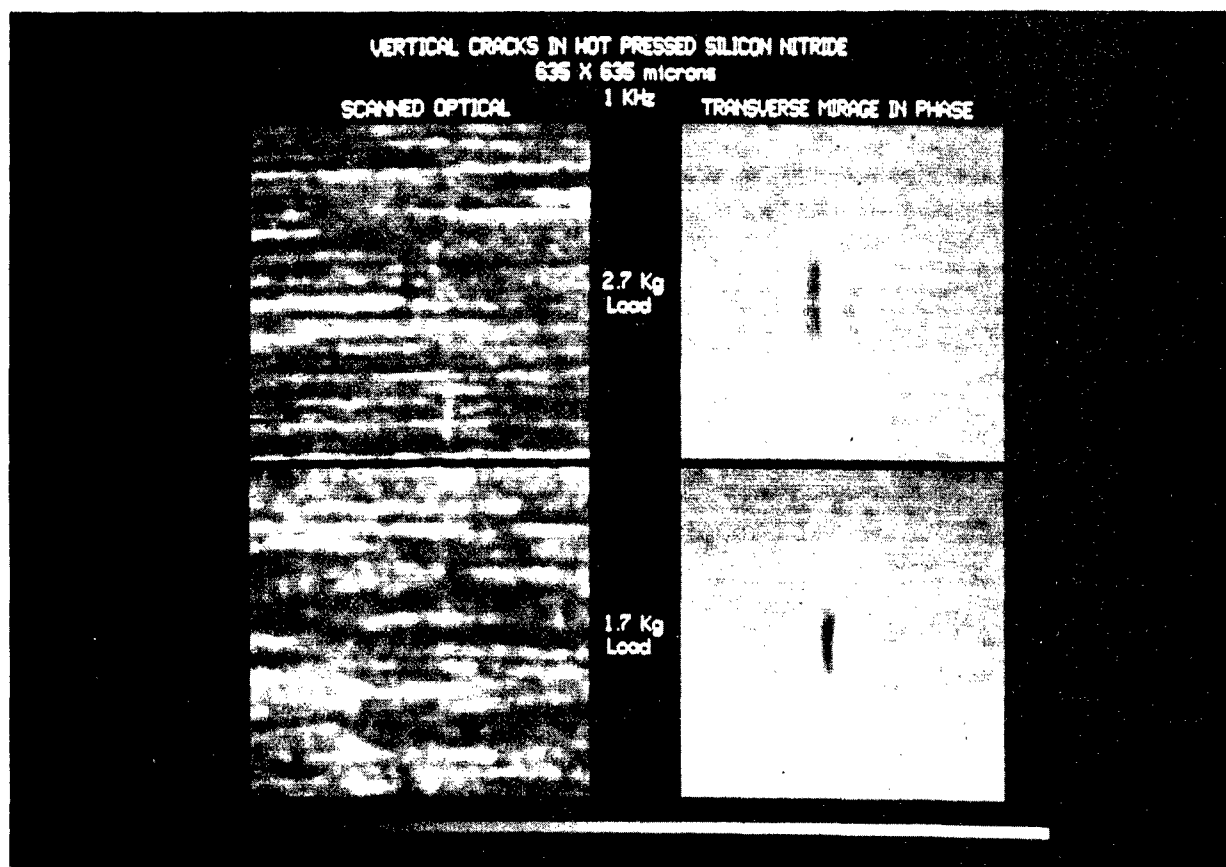


Fig. 35. Thermal wave MIRAGE (in-phase component of the transverse deflection at 1 kHz) and scanned optical images for the Knoop indented surfaces of silicon nitride Specimen No. 4. [ top: 2.7 kG load indentation crack; bottom: 1.7 kG load indentation crack].

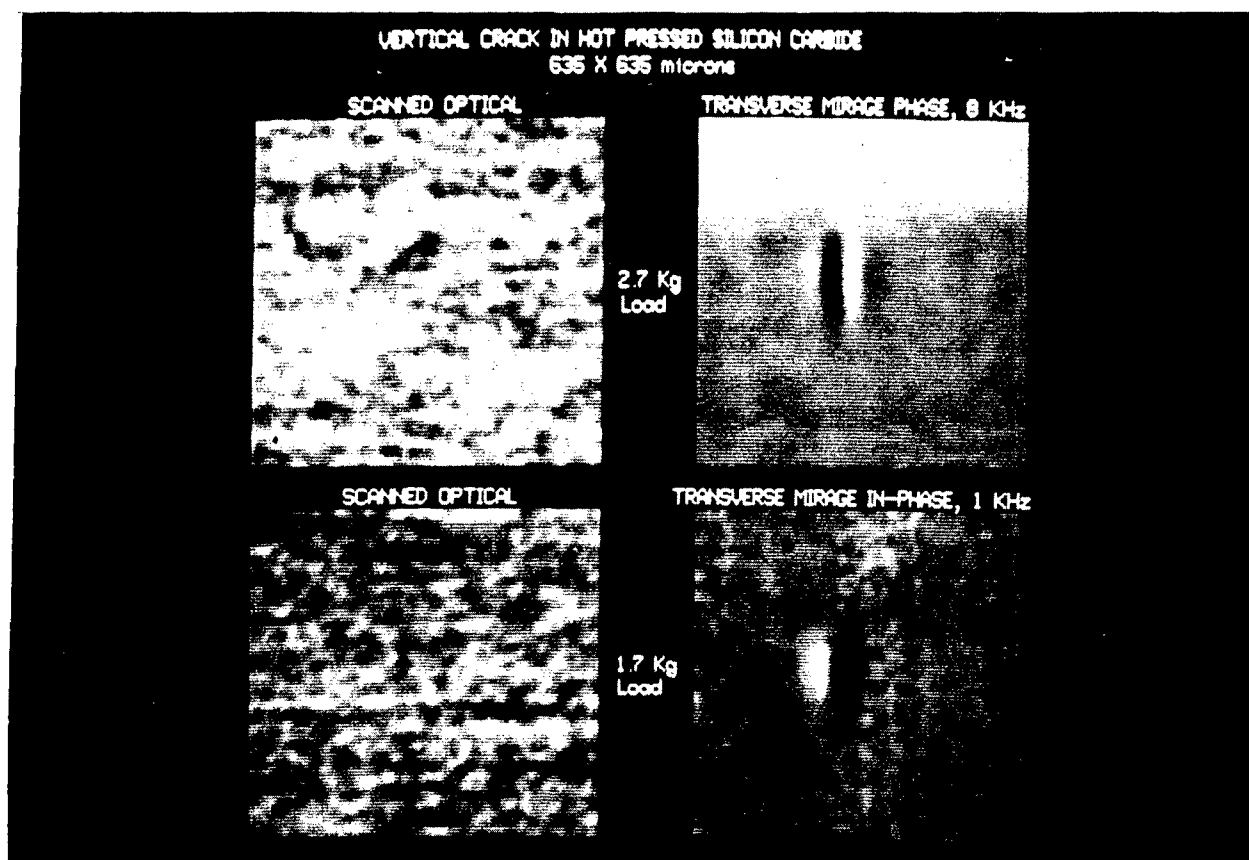


Fig. 36. Thermal wave MIRAGE (phase [top], in-phase component [bottom] of the transverse deflection at 1kHz) with scanned optical images for the Knoop indented surfaces of silicon carbide Specimen No. 5. [top: 2.7 kG load indentation crack; bottom: 1.7 kG load indentation crack].

<u>SAMPLE</u>	<u>LOAD</u>	<u>OPTICAL LENGTH*</u>	<u>DEPTH**</u>	<u>THERMAL LENGTH</u>
Silicon Nitride	2.7 kg	140μm	70μm	152μm
	1.7 kg	110μm	50μm	114μm
Silcicon Carbide	2.7 kg	130μm	70μm	153μm
	1.7 kg	130μm	50μm	114μm

\* indicates that the measurement was made before the surface structure was machined away

\*\* estimated

Table 1. A table of ceramic samples used in vertical crack studies, and the optically and thermally measured crack dimensions. The thermal length is measured from both line traces and area scan images and is the distance measured from the start of the signal due to the crack to the last line containing a signal due to the crack.



values), with correspondingly poor signal-to-noise ratios. The authors recommend that further studies be made using a simple measurement of the thermal diffusivity for different regions of a given sample, and then for samples of different known mechanical properties. Such a study would assess the possibility that the variations in mechanical properties might correlate with variations in locally averaged thermal properties.

#### 6.2. Ceramic-coated Samples.

The results of these studies suggest that further systematic work on the MIRAGE technique as applied to thermal diffusivity measurements could be very useful in characterizing coatings. Both experiments and theory will be required. The observed frequency dependences for this series of coatings has indicated sensitivity both to the nature and thickness of the coating and also to the relative thermal properties of the substrate. Imaging of defects at the interface also should be possible.

#### 6.3. Hollow Turbine Blades.

Both theory and experiment are now well understood for the case of a cylindrical subsurface hole parallel to the surface of a metal alloy. Such a hole can be detected thermally from the top surface, provided that its shallowest surface is within about one thermal diffusion length (controllable by changing the frequency of the thermal wave) of the top surface. Resolution of progressively deeper regions of the cylindrical wall deteriorates rapidly because of the exponential decay of the thermal waves.

#### 6.4. Monolithic $\text{Si}_3\text{N}_4$ and SiC Samples.

The results of these studies have been encouraging. The transverse deflection MIRAGE technique is easily capable of detecting small, vertical, 'half-penny-shaped' cracks in these ceramics. It also seems likely that our thermal wave images of the heat-treated silicon nitride specimen have detected the expected small pits from surface oxidation. The results on the surface machining damaged samples are less conclusive. Although the damage is observed thermally, quantitative comparison with the degree of damage would be difficult on the basis of these images alone. Further studies of machining damage as well as heat-treated samples are recommended.

# LIST OF REFERENCES

1. Y.H. Wong, R.L. Thomas and G.F. Hawkins, Appl. Phys. Lett. 32, 538 (1978).
2. G. Busse, Appl. Phys. Lett. 35, 759 (1979).
3. J.J. Pouch, R.L. Thomas, Y.H. Wong, J. Schuldies, and J. Srinivasan, J. Opt. Am. 70, 562 (1980).
4. A. Rosencwaig, J. Appl. Phys. 51, 2210 (1980).
5. R.L. Thomas, J.J. Pouch, Y.H. Wong, L.D. Favro, P.K. Kuo, and A. Rosencwaig, J. Appl. Phys. 51, 1152 (1980).
6. L.D. Favro, P.K. Kuo, J.J. Pouch, and R.L. Thomas, Appl. Phys. Lett. 36, 953 (1980).
7. R.L. Thomas, L.D. Favro, L.J. Inglehart, P.K. Kuo, J. Lhota, and G. Busse, Proc. 1982 IEEE Ultrasonics Symposium, B. R. McAvoy, Ed., p.586.
8. L.D. Favro, P.K. Kuo, L.J. Inglehart, R.L. Thomas, and M. Srinivasan, J. Appl. Phys. 53, 1258 (1982).
9. K.R. Grice, L.J. Inglehart, L.D. Favro, P.K. Kuo, and R.L. Thomas, J. Appl. Phys. 54, 6245 (1983); P.K. Khandelwal, R.R. Kinnick, and P.W. Heitman, Bul. Am. Cer. Soc. 64, 1112 (1985).
10. L.J. Inglehart, R.L. Thomas, and J. Schuldies, J. Nondes. Eval. 1, 287 (1980).
11. G. Busse, Appl. Opt. 21, 107 (1982).
12. R.L. Thomas, L.D. Favro, P.K. Kuo, and D.N. Rose, US Army Tank-Automotive Command Research and Development Center Technical Report No. 12668, Warren, MI 48090, July 1982.
13. R.L. Thomas, L.D. Favro, P.K. Kuo, D.N. Rose, D.Bryk, M. Chaika, and J. Patt, US Army Tank-Automotive Command Research and Development Center Technical Report No. 12957, Warren, MI 48090, June 1984.
14. R.L. Thomas, L.J. Inglehart, M.J. Lin, L.D. Favro, and P.K. Kuo, Review of Progress in Quantitative Nondestructive Evaluation, D.O. Thompson and D. Chimenti, Eds., Vol. 4B, p. 859 Plenum (1985).
15. L.J. Inglehart, D.J. Thomas, M.J. Lin, L.D. Favro, P.K. Kuo, and R.L. Thomas, Review of Progress in Quantitative Nondestructive Evaluation, D.O. Thompson and D. Chimenti, Eds., Vol. 4B, p. 753 Plenum (1985).

# Distribution List

No. of Copies

Commander, U.S. Army Tank-Automotive Command  
Warren, MI 48397-5000

ATTN: AMSTA-R, Col J. H. Van Zandt, Jr.	1
AMSTA-RS, Mr. Don W. Rees	1
AMSTA-RSA, Dr. Grant Gerhart	1
AMSTA-RTT, Mr. Jacob Patt	1
AMSTA-QAT, Mr. Foster Brown	2
AMSTA-RCM, Mr. S. A. Catalano	1
AMSTA-RGET, Dr. Richard Munt	1
AMSTA-RGED, Dr. Walter Bryzik	1
AMSTA-RGET, Mr. John Lewakowski	1
AMSTA-TMM, Ms. Jan Dentel	1
AMSTA-TBM, Mr. William Moncrief	1
AMSTA-TSL	2

Director, U.S. Army Materials Technology Laboratory  
Watertown, MA 02171-0001

ATTN: AMXMR-EM, Mr. Perry R. Smoot	1
AMXMR-MI, Dr. Al Broz	1
AMXMR-CO, Dr. R. N. Katz	1
AMXMR-STM, Mr. Paul Doyle	1
AMXMR-STM, Mr. Jim Kidd	1
AMXMR-MCP, Dr. George Quinn	1
AMXMR-OP, Dr. Robert E. Singler	1
AMXMR-MCP, Dr. Dennis Viechniechi	1
AMXMR-OM, Mr. Charles Gazzara	1
AMXMR-OP, Dr. James W. McCauley	1
AMXMR-OC, Dr. Janet Perkins	1
AMXMR-OP, Dr. Wensel Davidson	1
AMXMR-STQ, Mr. Fred Stinton	1
AMXMR-OM, Mr. Forrest Burns	1
SLCMT-MS, Mr. Paul W. Rolston	1
SLMT-MSI-NE, Mr. Robert Brockelman	1

Commander, U.S. Army Research Office  
P. O. Box 12211

Research Triangle Park, NC 27709	
ATTN: Dr. George Mayer	1
Dr. Frederick Rothwarf	1
Dr. Andrew Crowson	1
Dr. Mack Mellor	1

Commander, Naval Coastal Systems Center

ATTN: Code 715, Mr. Steve Gorin	1
Panama City, FL 32407	

No. of Copies

Commander, U.S. Army Mobility Equipment R&D Command ATTN: AMDME-WC (Tech Library) Fort Belvoir, VA 22060	1
Commander, Defense Technical Information Center ATTN: Bldg 5, DDAC Cameron Station Alexandria, VA 22314	12
Commander, U.S. Army Foreign Science & Technology Center ATTN: AMXST-CE Charlottesville, VA 29902	1
Commander, U.S. Army Missile Command ATTN: AMSMI-YM Redstone Arsenal, AL 35898	1
Commander, Harry Diamond Laboratories ATTN: DELHD-TD 2800 Powder Mill Road Adelphi, MD 20783	1
Dr. Robert P. Walson Cummins Engine Company, Inc. Mail Code 50165 Box 3005 Columbus, IN 47201	1
Mr. Alex Vary, Head Nondestructive Evaluation Section Materials Division MS 106-1 National Aeronautics and Space Administration Lewis Research Center 21000 Brookpark Road Cleveland, OH 44135	1
Mr. Alan R. Hirasuma L'Garde, Inc 1555 Placentia Avenue Newport Beach, CA 92663	1
Dr. David Dwight 210 Holden Hall Materials Engineering Virginia Polytechnic Institute and State University Blacksburg, VA 24061	1

No. of Copies

Mr. John M. Corwin Research Office Chrysler Corporation P. O. Box 1118 Detroit, MI 48288	1
Mr. John E. Becker ATTN: STRBE-L U.S. Army Belvoir Research & Development Center Ft. Belvoir, VA 22060	1
Dr. Harry Ringermacher United Technologies Research Center East Hartford, CT 06108	1
Prof. John Murphy Johns Hopkins Applied Physics Laboratory The Johns Hopkins University Johns Hopkins Road Laurel, MD 20810	1
Dr. Jacob Stiglich Aerojet Ordnance Co. 2521 Michelle Drive Tustin, CA 92680	1
Dr. James M. Toth Research Center Republic Steel Corp. 6801 Brecksville Road Cleveland, OH 44135	1
Dr. Ky Narasimham Spectra Research System Bldg. 860 Vandenburg AFB, CA 93437	1
Dr. Robert V. Ieth, Chief Scientist Div. 76 Hughes Aircraft P.O. Box 902 El Segundo, CA 90245	1
Dr. Thomas J. Moran AFWAL/MLLP Wright Patterson AFB, OH 45433	1

	<u>No of Copies</u>
Dr. M. Srinivasan Sohio Electro Minerals Company Advanced Materials Division P.O. Box 832 Niagara Falls, NY 14302	1
Dr. David W. Oliver General Electric Bldg. 37, Rm. 251 Schenectady, NY 12345	1
Dr. Vicki Panhuisse Garrett Turbine Engine Company P. O. Box 5217 Phoenix, AZ 85010	1
Dr. Pramod Khandelwal Allison Gas Turbines P. O. Box 420, Mail Stop W-5 Indianapolis, Indiana 46206	1
Mr. Dennis Hornberger Sermetel, Inc. 155 South Limerick Road Limerick, PA 19468	1
Dr. Dale Chimenti AFWAL/MLLP Wright Patterson AFB, OH 45433	1
Dr. Darryl P. Almond School of Materials Science University of Bath Cloverton Down Bath BA27AY Avon England	1
Mr. Ken Fizer Code 341 Naval Air Rework Facility Norfolk, VA 23511	1
Mr. George Lukes U.S. Army Engineering Topographical Laboratory Research Institute Ft. Belvoir, VA 22060	1

No. of Copies

Dr. Tung-Ho Chen AMCCOM, ARDC EMD, Bldg. 3028 Dover, NJ 07801	1
Dr. Philip F. Kalina Central Research Inorganic Laboratory M.E. Pruitt Building (1776) Midland, MI 48460	1
Dr. Keith O. Legg Ionic Atlanta, Inc. 1347 Spring St., NW Atlanta, GA 30309	1
Mr. David M. Barrett Battelle Columbus Laboratories 505 King Avenue Columbus, OH 43201	1
Col Ken Grice Dept of Physics U.S. Military Academy West Point, NY 10996	1
Mr. Al Frazer, Marketing Manager Electrooptical and Data System Group P. O. Box 902 El Segundo, CA 90245	1
Commander, U.S. Army Armament, Munitions and Chemical Command Benet Weapons Laboratory Watervliet, NY 12189 ATTN: Mr. Julius Frankel, Bldg. 115 Dr. M. H. Kamdar, Bldg. 115 Mr. Rick Campolini, SARWV-QAE, Bldg. 44	1 1 1
Mr. Henry Hartmann U.S. Army AMCCOM (D) ATTN: B19, NDT Lab Dover, NJ 07801	1
Dr. Gary F. Hawkins Aerospace Corporation MS-M2-250 P. O. Box 92957 Los Angeles, CA 90009	1

	<u>No. of Copies</u>
Dr. Jim Lhota Aerospace Corporation MS-M2-250 P. O. Box 92957 Los Angeles, CA 90009	1
Mr. Lewis J. Swank Ford Motor Co. Room E3172 SRL P. O. Box 2053 Dearborn, MI 48121	1
Mr. Michael Deluca PCK Technology 322 L.I.E. Drive Melville, NY	1
Mr. John Zuccon Photoacoustic Laboratory Dept. of Mechanical Engineering University of Toronto Toronto, Ontario M551A4 CANADA	1
Dr. Christopher S. Berndt NASA-Lewis Research Center MS 105-1 2100 Brookpark Road Cleveland, OH 44135	1
Dr. Andrus Niller AMDAR-BLF (A), Bldg. 120 Ballistic Research Laboratory Aberdeen Proving Ground, MD 21005	1
Dr. Robert W. McClung Oak Ridge National Laboratory 4500-S, D-61, Box X Oak Ridge, TN 37831	1
Dr. Robert E. Richards 3M Company New Products Department 219-01-01, 3M Center St. Paul, MN 55144	1
Dr. Clay O. Ruud The Pennsylvania State University 159 Materials Research Laboratory University Park, PA 16802	1



	<u>No. of Copies</u>
Dr. Wayne K. Stuckey The Aerospace Corporation P. O. Box 92957, MS M2/250 Los Angeles, CA 90009	1
Dr. John B. Wachtman, Jr. Rutgers University Director, Center for Ceramics Research Room A274, P. O. Box 909 Piscataway, NJ 08854	1
Dr. James R. Wilshire Headquarters, Department of the Army ATTN: DALO-PLO Rm. 2C-556 Washington, DC 20310	1
Mr. Fred Michel AMCMT U.S. Army Material Command 5001 Eisenhower Avenue Alexandria, VA 22333	1
Mr. Mark Schumacher ATTN: MS971 Texas Instruments, Inc. 13500 N. Central Expressway Dallas, TX 75265	1
Mr. Walt Dudley Monsanto Research Corp. Mound Lab Mound Road Miamisburg, OH 45342	1
Dr. Chuck Woods Monsanto Research Corp. Mound Lab Mound Road Miamisburg, OH 45342	1
Dr. Richard S. Quimby Physics Dept. Worcester Polytechnic Institute Worcester, MA 01609	1

No. of Copies

Dr. Takehiko Kitamori  
Energy Research Laboratory, 1168 Moriyama  
Hitachi, Ibaraki  
316 JAPAN

1

Dr. Tomoharu Watanabe  
Department of Industrial Chemistry  
Faculty of Engineering  
University of Tokyo, 7-3-1 Hongo  
Bunkyo-ku, Tokyo  
JAPAN.113

1

Dr. M. Kasai  
Department of Industrial Chemistry  
Faculty of Engineering  
University of Tokyo, 7-3-1 Hongo  
Bunkyo-ku, Tokyo  
JAPAN.113

1

Dr. T. Sawada  
Department of Industrial Chemistry  
Faculty of Engineering  
University of Tokyo, 7-3-1 Hongo  
Bunkyo-ku, Tokyo  
JAPAN.113

1

Dr. Y. -C. Yang  
Geo-Centers, Inc. 47 Auth Place  
Suitland, MD 21014

1

Ms. Peg Weeks  
McMahon Hall  
Alfred University  
Alfred, NY 14802

1

Mr. Xavier Maldague  
National Research Council  
75 de Mortagne  
Boucherville, Quebec  
CANADA J4B 6Y4

1

Mr. Eric S. Lillybeck  
San Fernando Laboratories 10258 Norris Avenue  
Pacoima, CA 91331

1

Manager, Defense Logistics Studies Information Exchange ATTN: AMXMC-D Fort Lee, VA 23801	1
Mr. Frederick J. Dudek 50 UOP Plaza Des Plaines, IL 60016-6187	1
Dr. Stephen T. Gonczy 50 UOP Plaza Des Plaines, IL 60016-6187	1
Mr. Noam Arnon Ceramic Materials Department Ford Motor Company P. O. Box 2053 Dearborn, MI 48121	1
Dr. David W. Richerson Director, Research & Development Ceramatec, Inc. 163 West 1700 South Salt Lake City, Utah 84115	1
Dr. John Baker Unviersal Energy Systems 4401 Dayton-Xenia Road Dayton, OH 45432	1
Mr. Harold R. Turner School of Physics Georgia Institute of Technology Atlanta, GA 30332	1
Commander, U.S. Army Construction Engineering Research Laboratory Corps of Engineers P.O. Box 4005 Champaign, IL 61820-1305 ATTN: Engineering and Materials Division, Mr. Vince Hock	1

No. of Copies

Mr. James W. MacBeth Structural Ceramics Division Sohio Engineered Materials P.O. Box 1054 Niagara Falls, NY 14302	1
Dr. James W. Laughner New York State College of Ceramics Alfred University Alfred, NY 14802	1
Commander, US Army Ballistic Research Laboratory Aberdeen Proving Ground, MD 21005-5066 ATTN: AMXBR-SECAD, Dr. Mike Riley	1
Dr. William D. Friedman The Standard Oil Co. 4440 Warrensville Center Rd. Cleveland, OH 44128	1
Dr. B. K. Bein Rhur-Universitat Bochum Institut fur Experimentalphysik VI Gebäude NB Postfach 102148 4630 Bochum 1 Fed. Rep. of Germany	1